

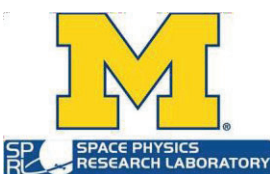
**CYCLONE GLOBAL NAVIGATION
SATELLITE SYSTEM (CYGNSS)**



**Algorithm Theoretical Basis Document
Level 1B DDM Calibration**

UM Doc. No.	148-0137
SwRI Doc. No.	N/A
Revision	Rev 4
Date	9 November 2021
Contract	NNL13AQ00C

Algorithm Theoretical Basis Documents (ATBDs) provide the physical and mathematical descriptions of the algorithms used in the generation of science data products. The ATBDs include a description of variance and uncertainty estimates and considerations of calibration and validation, exception control and diagnostics. Internal and external data flows are also described.



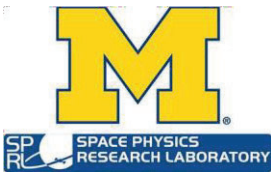
**CYCLONE GLOBAL NAVIGATION
SATELLITE SYSTEM (CYGNSS)**



**Algorithm Theoretical Basis Document
Level 1B DDM Calibration**

UM Doc. No.	148-0137
SwRI Doc. No.	N/A
Revision	Rev 4
Date	9 November 2021
Contract	NNL13AQ00C

Prepared by: Scott Gleason, Mohammad Al-Khaldi, Darren McKague November, 2021



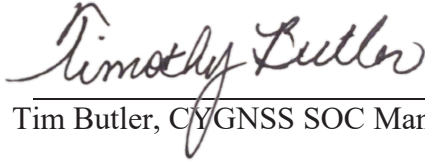
Approved
by:



Chris Ruf, CYGNSS Principal Investigator

Date: 9 Nov 2021

Approved
by:



Tim Butler, CYGNSS SOC Manager

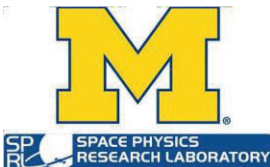
Date: 9 Nov 2021

Released
by:



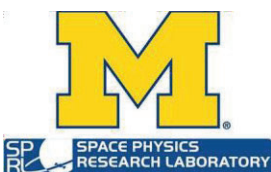
Darren McKague, CYGNSS UM Project Manager

Date: 9 Nov 2021



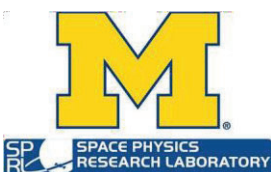
REVISION NOTICE

Document Revision History		
Revision	Date	Changes
PRE-RELEASE DRAFT	17 June 2013	n/a
INITIAL RELEASE	14 January 2014	Add unwrapping of the radar range equation to estimate normalized scattering cross-section from received power. Add detailed error analysis.
Rev 1	19 December 2014	Change L1b DDM units to scattering cross-section in meters ² . Add ancillary data product of scattering area in each DDM bin. Add greater detail about algorithm implementation.
Rev 2	20 August 2018	Inclusion of all modifications made to the Level 1A algorithms based on observed on-orbit performance between March 2017 and August 2018.
Rev 3	20 October 2020	Inclusion of all modifications for for zenith EIRP calibration.
Rev 4	8 November 2021	Inclusion of nadir and zenith bin ratio corrections, DDMA normalization area re-scaling, NBRCS normalization, and EIRP normalization.



Contents

LEVEL 1B CALIBRATION APPROACH.....	7
FORWARD MODEL OF SCATTERED SIGNAL POWER.....	7
GEOLOCATION OF SURFACE MEASUREMENT: SOLVING FOR THE SURFACE SPECULAR REFLECTION POINT	8
Mean Sea Surface Height Model	9
Specular Point Solver Implementation.....	10
LEVEL 1B CALIBRATION ALGORITHM: WATTS TO SIGMA0.....	12
Expression For Bi-static Radar Cross Section	12
Calculating Effective and Physical Scattering Areas	14
Digital to Analog DDM Scaling Issue	15
Calculating a Normalized Bi-static Radar Cross Section.....	16
Altitude Dependant DDMA Area Normalization	17
Characterization of GPS Effective Isotropic Radiated Power (EIRP, v2.1 calibration)	20
Zenith EIRP Calibration (Version 3.0 calibration)	23
Rescaling of Nadir Antenna Patterns	26
NBRCS and EIRP Normalization.....	34
CYGNSS LEVEL 1 ERROR ESTIMATION METHOD.....	35
Error Analysis Methodology.....	36
Rolled Up On-Orbit Level 1 Calibration Errors	36
Rolled up L1 Uncertainty.....	37
CYGNSS Level 1 Bin Ratio Correction	38
CYGNSS Analog to Digital Convertor (ADC) Design	38
Impact of On-Orbit Bin Ratio Fluctuations on L1 Calibration.....	39
Nadir Bin Ratio Correction.....	40
Zenith Bin Ratio Correction.....	42
DDMA normalization area re-scaling.....	44
REFERENCES	47
Appendix – Level 1 Data Dictionary	49





LEVEL 1B CALIBRATION APPROACH

This document is the second part of the overall Level 1 Calibration Algorithm Theoretical Basis Document (ATBD) describing the Level 1b calibration. Portions of this ATBD have been re-published in [1].

The Level 1b calibration is performed after the Level 1a calibration and will use external meta-data to convert the Level 1a mapped power in Watts to a delay Doppler map (DDM) map of normalized bistatic radar cross section (NBRCS) values. This conversion will be done for every pixel in every DDM and requires the following information at the time the science DDM is collected,

- 1) The CYGNSS satellite GPS time, position and velocity in the WGS84 Earth Centered Earth fixed (ECEF) reference frame.
- 2) The GPS satellite position and velocity in the Earth WGS84 Centered Earth fixed (ECEF) reference frame.
- 3) Detailed knowledge of the CYGNSS nadir antenna gain patterns.
- 4) Best estimated attitude knowledge of the CYGNSS spacecraft at the time of the measurement.
- 5) An estimate of the GPS effective isotropic radiative power (EIRP) in the direction of the specular reflection point in the GPS satellite reference frame.

Additional information calculated using the per DDM science meta data and used in the Level 1b calibration of each

DDM includes,

- 1) An accurate surface geolocation of the reflection specular point (SP) in the WGS84 ECEF reference frame.
- 2) A precise estimate of the specular reflection point location in the measurement DDM pixel delay and Doppler bins.
- 3) The path length between the GPS satellite and specular reflection point and between the specular reflection point and the CYGNSS spacecraft making the measurement.
- 4) The effective scattering area per DDM bin surrounding the specular point over all delay and Doppler bins.

The above parameters are then used to estimate values of the bistatic radar cross section for each DDM pixel using the forward model described below.

FORWARD MODEL OF SCATTERED SIGNAL POWER

A full expression for the GPS scattered signal power has been previously derived and published in 2000 [2], shown in Equation 1. The original representation has been slightly modified in form and variable names,

$$P_{\hat{\tau},\hat{f}}^g = \frac{P^T \lambda^2}{(4\pi)^3} \iint_A \frac{G_{x,y}^T \sigma_{x,y}^0 G_{x,y}^R}{(R_{x,y}^R)^2 (R_{x,y}^T)^2} \Lambda_{\hat{\tau};x,y}^2 S_{\hat{f};x,y}^2 dx dy \quad (1)$$

where $P_{\hat{\tau},\hat{f}}^g$ is the coherently processed scattered signal power, in Watts. P^T is the GPS satellite transmit power and $G_{x,y}^T$



is the GPS satellite antenna gain. $G_{x,y}^R$ is the CYGNSS satellite receiver antenna gain. $R_{x,y}^T$ and $R_{x,y}^R$ are the transmitter to surface and surface to receiver ranges, respectfully. $\sigma_{x,y}^0$ is the normalized bistatic scattering cross section (NBRCS). λ is the GPS signal carrier wavelength (approx. 19 cm). $\Lambda_{\tau;x,y}$ is the GPS signal spreading function in delay and $S_{\hat{f};x,y}$ is the frequency response of the GPS signal. A is the surface integration area covering the effective region of diffuse scattering for each delay Doppler bin. The scattered signal power is processed using a 1ms coherent integration intervals over a range of relative delays $\hat{\tau}$ and Doppler frequencies \hat{f} , followed by 1 second of non-coherent averaging. These delay and frequency bins map non-uniquely spatially to physical coordinates on the surface.

The above expression can be simplified using the effective values of several variables across delay and Doppler bins under the integrand of Equation 1. The effective values include the effects of delay and Doppler spreading functions, Λ and S , which have been eliminated from the Equation and are indicated by the over-bar in the following equations. The surface mapping from physical (x,y) coordinates to delay and Doppler coordinates reflects the actual processing as performed in the CYGNSS delay Doppler mapping instrument (DDMI).

$$P_{\hat{\tau}, \hat{f}}^g = \frac{P^T \lambda^2 G_{\hat{\tau}, \hat{f}}^T \langle \sigma_{\hat{\tau}, \hat{f}}^0 \rangle \bar{G}_{\hat{\tau}, \hat{f}}^R \bar{A}_{\hat{\tau}, \hat{f}}}{R_{\hat{\tau}, \hat{f}}^T R_{\hat{\tau}, \hat{f}}^R} \quad (4\pi)^3 (\bar{R}_{\hat{\tau}, \hat{f}})^2 (\bar{R}_{\hat{\tau}, \hat{f}})^2 \quad (2)$$

where, $\bar{G}_{\hat{\tau}, \hat{f}}^R$ = The effective receiver antenna gain at each delay/Doppler bin. $\bar{R}_{\hat{\tau}, \hat{f}}^T$ and $\bar{R}_{\hat{\tau}, \hat{f}}^R$ are the effective range losses at each delay/Doppler bin and $\bar{A}_{\hat{\tau}, \hat{f}}$ is the effective surface scattering area at each delay/Doppler bin.

All variables in Equation 2 vary with respect to delay $\hat{\tau}$ and Doppler \hat{f} (which map to the x,y surface grid over the glistening zone), however, for the sake of simplification and with negligible loss in accuracy, several parameters can be estimated and applied as constants across the DDM measurement as expressed below.

GEOLOCATION OF SURFACE MEASUREMENT: SOLVING FOR THE SURFACE SPECULAR REFLECTION POINT

The estimated location of the center of the surface glistening zone of the reflected signal provides the main point of reference for the geo-location of the GNSS-R measurement. This point on the surface is referred to as the specular point and can be estimated mathematically using the physical geometry of the transmitting and receiving satellites and a modeled of the Earth’s ocean surface. It should be noted that the surface specular point estimation algorithm described below is designed for ocean surfaces. Land specular points over varying topography present unique challenges and will contain additional geolocation errors, not yet accounted for in the current CYGNSS Level 1 calibration.

In the original Level 1 calibration approach, the specular point was solved using a) the position of the receiving satellite, as estimated by the 1Hz single frequency position estimate, b) the estimate of the transmitting satellite using ground based precise ephemeris and c) the WGS84 ellipsoid model of the Earth. This Earth model, although generally accurate enough for most applications, relied on approximations that resulted in residual specular point position estimation errors that were large enough to significantly impact the pixels in the DDM used to calculate the bistatic radar cross section. Subsequently, an improved specular point solver was implemented that used a more accurate DTU10



mean sea surface model [3], combined with a brute force, computationally-efficient specular point solver algorithm.

The specular point on the Earth maps to a single point in the delay-Doppler coordinates in the CYGNSS DDM. The exact specular bin location in the DDM will be located at a fractional pixel location within a single DDM bin. The pixels in the DDM at and surrounding the specular point bin determine the region used to make the surface bistatic radar cross section measurement, the DDMA. The estimation of the DDMA within the Level 1a DDM is described in more detail below using the precise location of the specular point described here. This region of the DDM represents the bins of highest reflected power and smallest spatial footprint on the surface and accurate knowledge of this regions is critical for calibration and wind speed retrievals.

The specular point location on the surface can't be reliably estimated using the peak power bin of the DDM. The peak power pixel results from a combination of effects in addition to the specular point location, including thermal noise, speckle noise or asymmetries in the reflected signal waveform (as a result of geometry and antenna pattern non-uniformity). For this reason, the specular point surface location and location of the specular point in the instrument generated DDM is calculated to a sub-pixel level from first principles (i.e. geometry and timing metadata).

Mean Sea Surface Height Model

In order to more precisely predict the specular location, it is necessary to account for deviations in the Earth's mean sea surface height as compared to the WGS84 model. For this purpose, we have utilized the DTU10 mean sea surface model [3]. The mean sea surface is the displacement of the sea surface relative to a mathematical model of the Earth and it closely follows the Earth's geoid. The amplitude of the deviation from the WGS84 ellipsoid is generally within approximately +/-100 meters over the Earth's ocean surfaces. The original DTU10 data was reduced to a 1 degree by 1 degree resolution to improve the efficiency of the calculation, and which is reasonable, due to the fact that height variations are relatively small. The DTU10 map of sea surface height variations relative to the WGS84 ellipsoid use in the specular point solver is shown in Figure 1.

The path delay error manifests itself as an error in the predicted reflection path delay, which, in turn, becomes an error in the predicted location of the specular bin in the DDM. The error in predicted path delay can be expressed as,

$$\rho = 2\cos(\theta)\delta h \quad (3)$$

Where ρ is the path delay error, θ is the reflection incidence angle and δh is the relative surface height error with respect to the WGS84 ellipsoid.

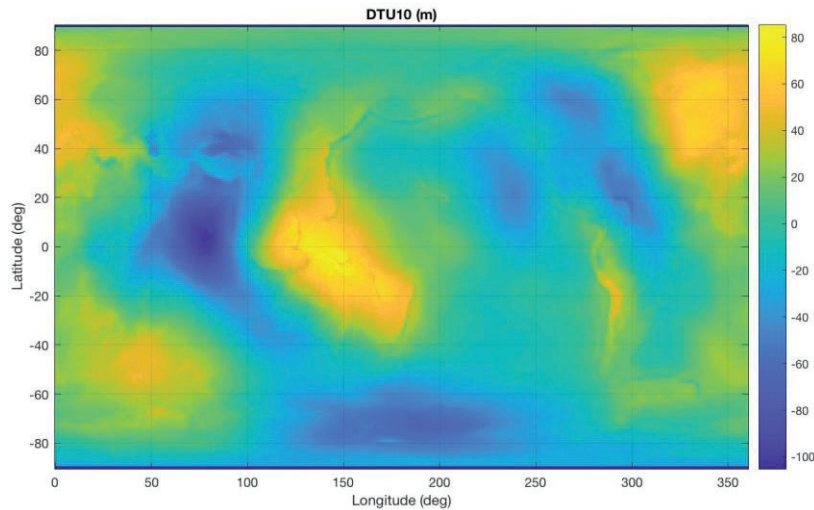


Fig. 1. DTU10 Mean Sea Surface data used for specular point calculation.

The height difference, manifests as a path delay error which becomes an error in the predicted location of the specular bin in the DDM. For a typical incidence angle of 30 degrees, a surface height error of 100 meters could result in 170 meters of path delay error. In the CYGNSS DDM, the delay pixel resolution is approximately 0.25 GPS L1 C/A code chips, and one chip corresponds to approximately 293 meters of delay. Therefore, a 170 m path delay error results in the predicted specular bin in the DDM being offset by 2.25 pixels from where we would expect it on the WGS84 ellipsoid.

Figure 2 shows a plot of specular bin delay difference when using DTU10 as opposed to using WGS84. Specular delay differences are shown for 1 day of measurements for 4 satellites (each shown in 4 separate colors). We can observe that the delay difference (or correction) due to the improved specular point solver varies between -2 and 2.5 pixels in delay space in the DDM. Figure 2 also shows an example measured CYGNSS DDM. In the DDM, the original specular bin solved using WGS 84 model is shown as a red 'X' while the new specular bin solved using DTU10 is shown with a red square. Visually, it is clear the specular bin location calculated with DTU10 is at the correct location in the reflected waveform. Range errors introduced by incorrect specular point prediction primarily impact the L1 calibration due to misidentifying the correct specular point bins (and specular region reflected power) in the DDM measurements. These errors will also degrade the surface vertical ranging accuracy and horizontal geolocation if not corrected.

Specular Point Solver Implementation

The new specular point solution is reported in the CYGNSS Level 1 data in the form of the specular point position and velocity variables. It takes approximately 20 seconds to calculate one day of precise specular points within CYGNSS DDMs from one satellite (approximately 320000 DDMs). The new algorithm used to solve for the specular point is as follows:

- 1) The original specular point solution based on the WGS84 ellipsoid model is used as our initial estimate of the specular point.



- 2) A large 3-D grid of points is constructed around the estimated specular point. This grid has uniform latitude and longitude spacing and is conformal to the WGS84 ellipsoid at each point.
- 3) At each grid point, the DTU10 mean sea surface height is used to shift the altitude. The 1-degree resolution DTU10 data (shown above) is bi-linearly interpolated to find the altitude value at each grid point. The resulting grid is then conformal to the DTU10 surface
- 4) Next, the point in the grid with the minimum reflection path length (from transmitter to the grid point to the receiver) is found. This minimum-path-delay grid point becomes the new specular point location estimate.
- 5) An additional higher resolution grid is constructed around this estimated specular point location and steps 2-4 are repeated several times. In this way, a series of search grids sequentially zoom in on the estimated specular point. The choice of initial grid size and resolution are carefully chosen to prevent erroneous convergence.

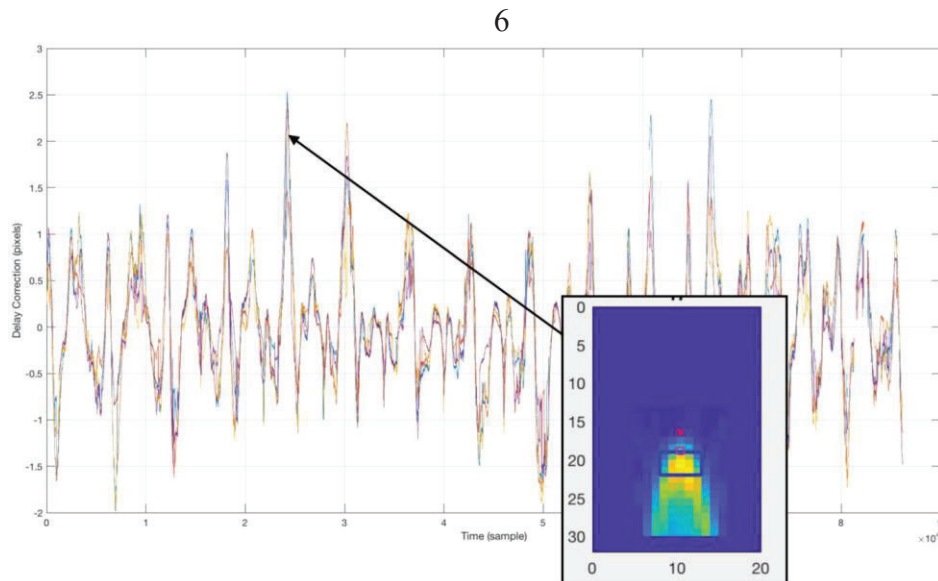


Fig. 2. One day of specular point corrections using the DTU10 model as compared to the WGS84 model. The correction due to the improved specular point solver varies between -2 and 2.5 pixels in delay space in the DDM.

The specular point we solve for here is defined as the point on the Earth with the minimum reflection path delay. As the surface we use is conformal to an arbitrary geoid topology at each grid point, no mathematical constraint is placed on transmitter and receiver incidence angles in this solution. In a strict sense, it is no longer a "specular" point since (if the ocean surface were smooth) a specular reflection would occur at surface locations with equal transmitter and receiver incidence angles, not minimum delay. Nonetheless, the minimum delay point is sufficiently relevant for our purposes since the corresponding specular bin defines the leading edge of the reflected waveform and the specular point represents the center of our iso-delay surface contours within the reflection glistening zone.



The DTU10 mean surface height model contains data over both ocean and land. The updated specular point estimates are valid and accurate over ocean only, as the DTU10 elevation model does not consider variations in land topography. An additional surface height map will be implemented in future versions of the L1 calibration which includes land surface height variations.

The updated specular point solution is differenced with the instrument estimated specular point solution to produce a correction term in the DDM's delay and Doppler space. This correction is applied to the original prediction of the specular bin location in the DDM during the estimation of the DDMA measurement area, as described in Section V(D).

LEVEL 1B CALIBRATION ALGORITHM: WATTS TO SIGMA0

The Level 1a calibrated DDM represents the received surface signal power in Watts binned over a range of time delays and Doppler frequencies. Before any geophysical parameters can be estimated these power values must be corrected for non-surface related terms by inverting the forward model shown in Equation 2. The CYGNSS Level 1b calibration generates three data products associated with each Level 1a DDM: 1) A bin by bin calculation of the surface bi-static scattering cross section, σ (not normalized by scattering area), 2) a bin by bin values of the effective scattering areas and 3) a NBRCS value for a DDM Area (DDMA) in a 3 delay x 5 Doppler bin region around the estimated specular point location in the DDM. The first two products will allow users to normalize values of σ to values of σ^0 (scattering cross section per meter squared), over configurable surface extents using summations of the effective scattering areas for individual DDM bins. The values of σ are corrected for the effects of the transmit and receive antennas, range losses and other non-surface related parameters. The effective scattering areas are calculated based on the measurement specific reflection geometry and include the GPS specific delay and Doppler spreading functions. However, care should be taken when using DDM bins away from the specular point, as some of the corrections applied (such as the receive antenna gain and path losses) will degrade at pixels outside the DDMA area. An overview of the CYGNSS Level 1b Calibration is shown in Figure 3.

Expression For Bi-static Radar Cross Section

The final expression for the Level 1b DDM can be derived from the expression of the signal forward model, expressed in Equation 2, by solving for the scattering cross section term, σ_0 . As the DDM Level 1b sigma product will not be

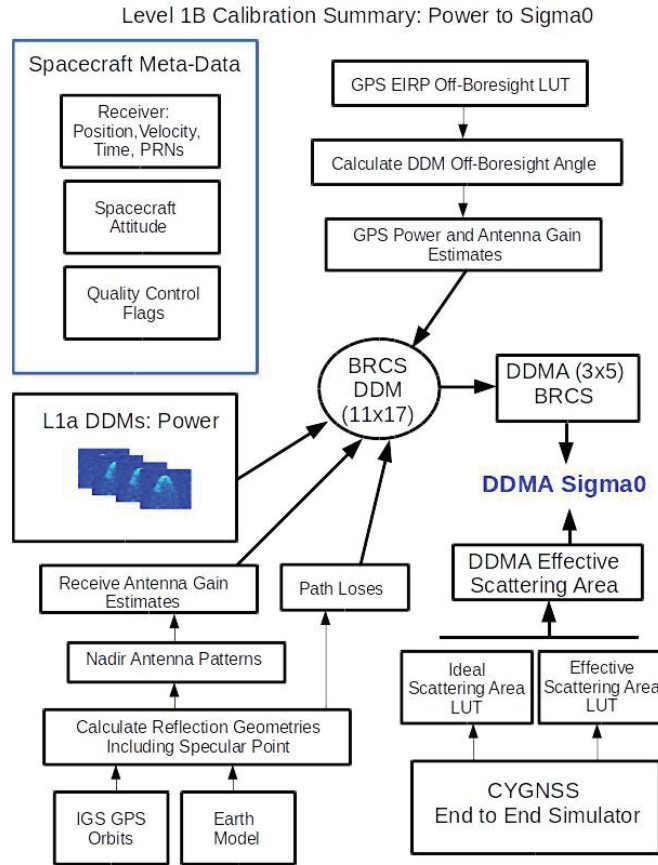


Fig. 3. Overview of CYGNSS Level 1b Calibration.

normalized, we have removed A^- from Equation 2 and replaced the normalized radar cross section σ^0 with the non normalized, σ . Additionally, Receive antenna gain G_{SP}^R , the GPS antenna gain G_S^T , and total path loss (simplified into a single value) R_S^{Total} terms are approximated with their values at the specular point and applied across the whole DDM. The resulting expression for the bin by bin scattering cross section, σ , is,

$$P_{\hat{\tau}, \hat{f}}^{L1b} = \langle \sigma_{\hat{\tau}, \hat{f}} \rangle = \frac{P_{\hat{\tau}, \hat{f}}^g (4\pi)^3}{P^T \lambda^2 G_{SP}^T G_{SP}^R R_{SP}^{Total}} \quad (4)$$

where the individual terms in Equation 4 are as follows,

- 1) $P_{\hat{\tau}, \hat{f}}^g$ is the Level 1a calibrated signal power at a specific delay ($\hat{\tau}$) and Doppler (\hat{f}) bin.
- 2) R_{SP}^{Total} is the total range loss from the transmitter to the surface and the surface to the receiver at the specular point. When using a relatively small area of of the DDM near the specular reflection point, this value can be approximated as the total range from the transmitter to the specular point to the receiver. This term is included in the denominator as it is calculated as a loss $R^{Total} = 1/(R^R)^2 * 1/(R^T)^2$



- 3) P^T and G_{SP}^T are the GPS satellite transmit power and antenna gain at the specular point. These values are estimated using a ground based GPS Power Monitor and measurements from the CYGNSS navigation antenna to map the transmit power of individual GPS satellites. Details can be found in [6].
- 4) G_{SP}^R is the receiver antenna gain at the specular point applied across all DDM bins. The SP antenna gain outside the DDMA region will introduce errors that should be accounted for when using pixels outside the DDMA region (3 delay and 5 Doppler around SP).

8

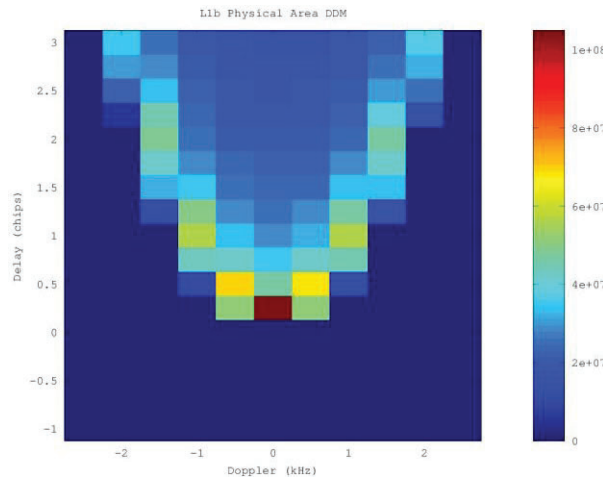


Fig. 4. Physical Scattering Area for a typical DDM reflection geometry. The delays before the specular reflection point do not correspond to any physical region on the surface.

Calculating Effective and Physical Scattering Areas

A single delay Doppler bin will contain the captured scattered power across one or more physical regions on the ocean surface. For each delay Doppler bin in the DDM this region will vary both in actual physical size (on the ground surface area) and effective area (combined with the GPS spreading functions). The GPS ambiguity functions (in both delay and Doppler) increase the effective area of each delay Doppler bin, causing power to be "spread" into adjacent delay and Doppler bins from outside the geometry determined physical scattering area. These functions change the levels of overall processed power observed. The physical area of each DDM bin can be calculated as follows,

$$A_{\tau, \hat{f}} = \iint_A dx dy \quad (5)$$

An example of the physical scattering area for a typical DDM is shown in Figure 4. Note that points up to and before the specular point bin (i.e. at delays shorter than the specular reflection point delay) have no physical surface scattering area. The power received in the bins before the specular point is due to power being spread into these bins by the GPS ambiguity functions from physical areas near the specular



point. The effective surface scattering area for each delay/Doppler bin is expressed as the ambiguity function weighted surface integration,

$$A^{-1}(\tau, f) = \frac{\iint \Lambda^2(\tau; x, y) S_f^2(f; x, y) dx dy}{A} \quad (6)$$

where the delay spreading function, $\Lambda_{\tau; x, y}$ and the Doppler spreading function, $S_{f; x, y}$, are integrated over the physical surface corresponding to each individual delay/Doppler bin. Figure 5 shows the effective scattering area DDM corresponding to the physical scattering areas illustrated in Figure 4.

Initial analysis has shown that when only using a relatively small area of the DDM (corresponding to approximately a 25km^2 area on the surface), it is sufficient to approximate the receive antenna gain, range loss terms and the GPS transmit antenna power and gain using constant values calculated at the specular reflection point.

As a standard Level 1 data product, CYGNSS data include DDMs over a 11 Doppler bins f and 17 delay (τ) pixels around the specular point. The NBRCS $\sigma_{\tau, f}$ is calculated as per Equation 4 for each delay/Doppler bin.

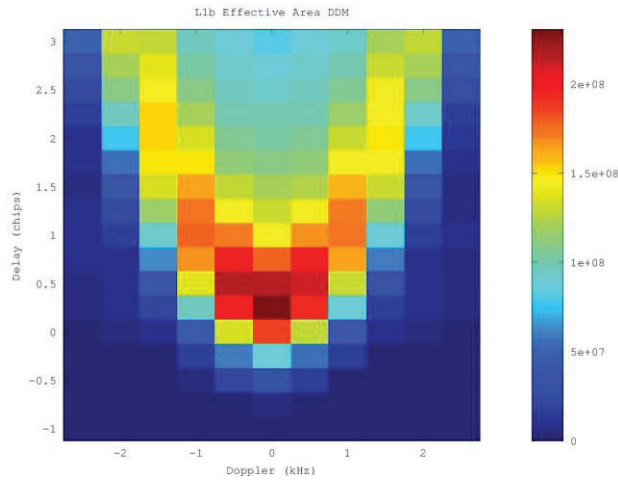


Fig. 5. Effective scattering area corresponding to the physical scattering area shown in Figure 4. This DDM of effective scattering area is a key output product of the Level 1b calibration which allows users to calculate normalized values of σ^0 .

Digital to Analog DDM Scaling Issue

In the original CYGNSS L1a calibration algorithm, the entire Level 1a DDM was scaled from digitally sampled DDM values to the equivalent analog sampled power based on the 2-bit analog to digital sample distribution. This correction was based on well-known methods in radio astronomy for dealing with finite



digital sampling of analog signals. However, examination of closely geo-located tracks between different observatories at very close time intervals revealed an observed bias between measurements over nearly identical conditions. Figure 8 (top) shows one such case, where FM6 and FM8 pass over nearly the same surface within 5 minutes of each other, yet a clear difference in the NBRCS values can be observed over the length of the track. Upon subsequent investigation, an issue in the analog to digital scaling being applied was found, in which the calculated correction between digital and analog measurements was not correct and introducing significant statistical biases between observatories.

Upon removal of the existing digital to analog scaling the overall inter-satellite bias statistics improved significantly. Figure 8 (bottom) shows the same two tracks after the scaling has been removed, with good agreement across the entire track.

The exact problem with the digital to analog scaling is being investigated and has not yet been identified. However, as a significant reduction in inter-satellite measurement bias was demonstrated with the removal of the digital to analog scaling factor, it will be included in the next public data release.

Calculating a Normalized Bi-static Radar Cross Section

The Level 1b bin by bin DDM of σ and the bin by bin DDM of effective scattering areas can be combined to calculate a normalized radar cross section value, σ^0 , over selected regions of the measurement DDM called the DDMA. The CYGNSS Level 2 wind retrieval products use the DDMA to generate geophysical model functions (GMF) to estimate near surface winds. The DDMA consists of 3 delay bins and 5 Doppler bins, with the specular point located in the first row (shortest delay) of this region. Figure 9 shows this DDMA region in red, overlapped with the normal instrument processed DDM delay and Doppler pixels in black. The true (best estimate) of the DDMA region (as calculated by the precise specular point estimation method described above) is marked as a red dot in this figure, while the white dot is the Level 1b DDM that the "true" specular point falls in.

These precise DDMA bins will not normally align exactly with the L1b DDM bins generated by the instrument (due to errors in the instruments open loop signal tracker) making a simple summation over 15 total bins in the L1b DDM problematic. The "true" DDMA radar cross section is the weighted combination of L1b DDM bins around the best estimate surface specular point and fractional contributions from bins around the edge of the DDMA region. This set of overlapping



DDM bins is, when weighted and summed, the best estimate of the "true" multi-bin DDMA total radar scattering cross section σ_0 . The mis-alignment between the measured L1b DDM bins and the "true" DDMA bins is illustrated in Figure 9. The DDMA specular point is offset by fractional bin amounts in delay (δ) and Doppler (Δ) from the L1b measurement DDM shown in the figure.

In order to calculate the total radar cross section in the red DDMA area, the actual measurement L1b values (one per white box/pixel) need to be combined using a weighting scheme that includes only a fractional amount of power from bins around the edges of the DDMA bins. The fractional weighting scheme used is approximated to be linear in both the delay and Doppler dimensions. Figure 9 shows the regions of overlap for a single red DDMA bin with respect to the surrounding measurement bin values.

The total DDMA radar cross section can be calculated as per Equation 8, resulting in a combined expression for the DDMA σ^0 ,

$$\sigma^0 = \frac{\sigma_{weighted}}{A_{total}} = \frac{W_{i,j} \sum_{i=1}^N \sum_{j=1}^M \sigma_{\tau_i, f_j}}{\sum_{i=1}^N \sum_{j=1}^M A_{\tau_i, f_j}} \quad (8)$$

where N and M represent the delay and Doppler bin in the L1b DDM, respectively (with N = 4 and M = 6, a single bin more than the DDMA size in both dimensions)

$$\begin{aligned} \sigma_{weighted} = & (1 - \delta)(1 - \Delta)\sigma_1 + (1 - \delta)(\sigma_2 + \sigma_3 + \sigma_4 + \sigma_5) \\ & + (1 - \delta)\Delta\sigma_6 + (1 - \Delta)(\sigma_7 + \sigma_{13}) + \Delta(\sigma_{12} + \sigma_{18}) \\ & + \delta(1 - \Delta)\sigma_{19} + \delta(\sigma_{20} + \sigma_{21} + \sigma_{22} + \sigma_{23}) + \delta\Delta\sigma_{24} \\ & + (\sigma_8 + \sigma_9 + \sigma_{10} + \sigma_{11}) + (\sigma_{14} + \sigma_{15} + \sigma_{16} + \sigma_{17}) \end{aligned} \quad (9)$$

Each bin in the L1b DDM contributing to the weighted $\sigma_{weighted}$ is scaled by a weighting factor $W_{i,j}$ based on the overlap with the respective "true" DDMA bin. $\sigma_{weighted}$ is then normalized by the sum of the effective area DDMA bins (which are centered at the ideal specular reflection point and require no weighting correction) to arrive at the final σ^0 measurement over the "true" DDMA region. The summations and weighting involved in calculating $\sigma_{weighted}$ for the example above is expressed in Equation 9, where the delay and Doppler index values are simplified to single bin numbers as illustrated in Figure 9, and terms with the same weighting factor are combined.

Altitude Dependant DDMA Area Normalization

The CYGNSS satellites were launched into slightly elliptical orbits, causing altitude fluctuations between perigee and apogee of up to approximately 35 km. This was not taken into account in the V2.0 calibration algorithm, where a circular orbit at a constant altitude was assumed during the generation of the initial look-up-tables (LUTs) used to perform the

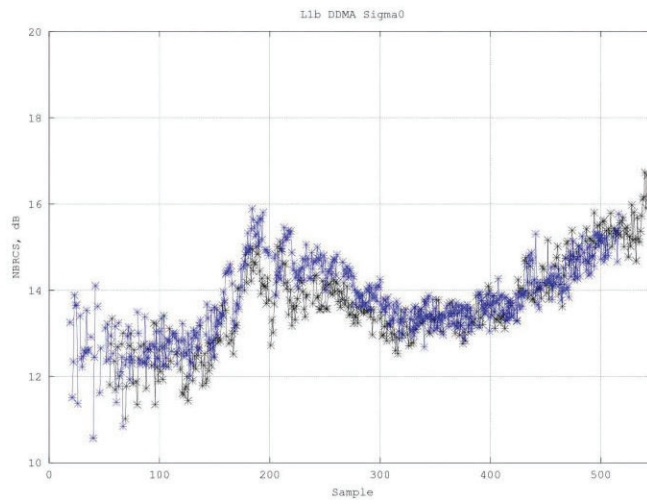
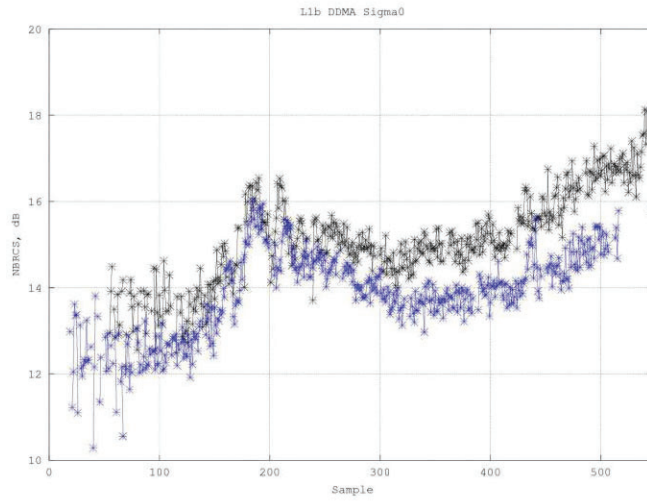




Fig. 8. (top) Inter-satellite bias between tracks of FM6 and FM8 on August 23rd less than 5 minutes apart. (bottom) After digital to analog scaling removed NBRCS values agree much better across the same ocean track.

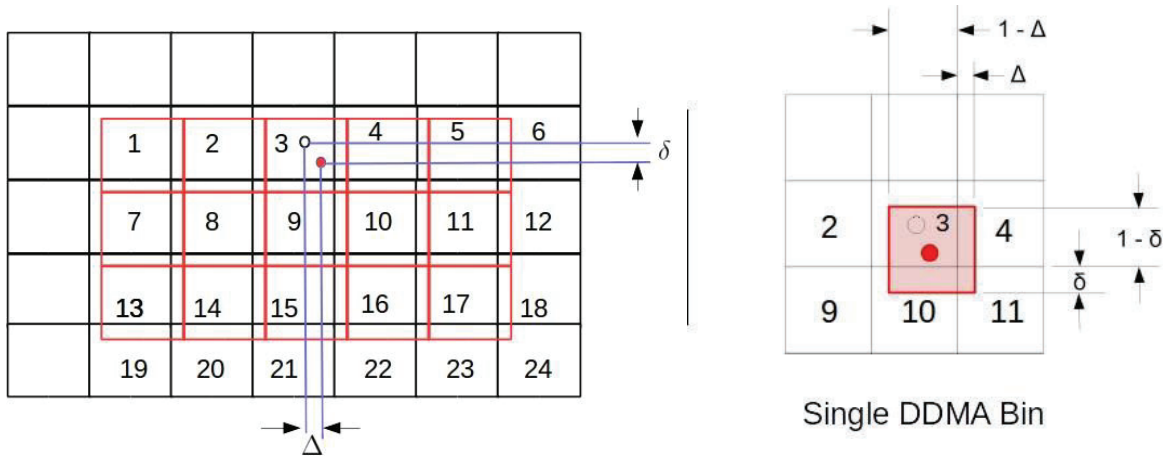


Fig. 9. (left) Level 1b DDM of σ values. Numbered to correspond to same pixels with DDMA overlayed and bin numbers referenced to Equation 9. The red group of DDMA bins is the overlay of the 3 by 5 DDMA measurement area with the processed Level 0 DDM pixels, containing a typical mis-alignment. The best estimate DDMA, is based on a refined specular point estimate and represents the true measurement error. (right) Detail of the overlap areas of a single DDMA bin (the specular point bin) and adjacent L1b bins.

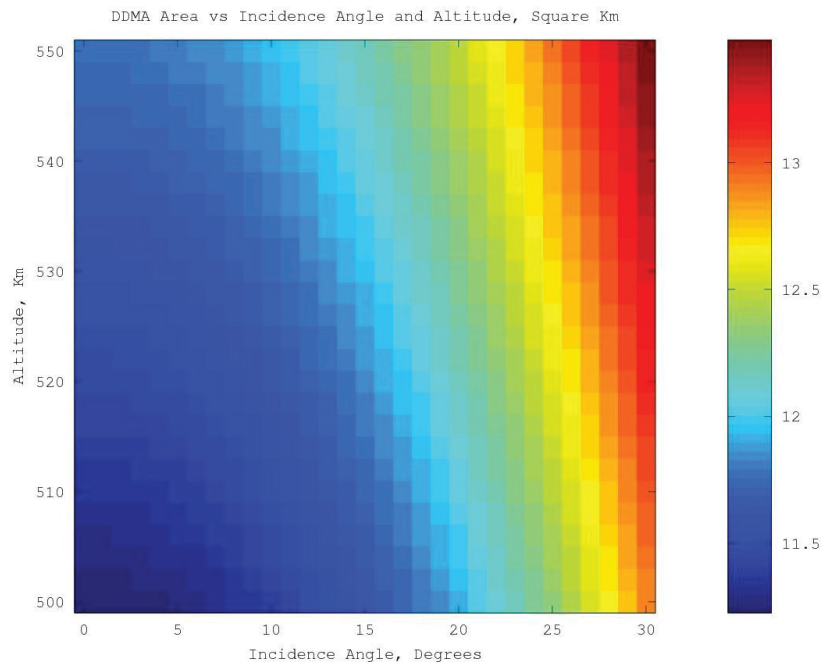


Fig. 10. Version 2.1 DDMA Area LUT values for altitudes between 500 and 550 km (covering the full range of the CYGNSS orbits, with margin on the low side), and incidence angles between 0 and 30 degrees. The increases in DDMA area with incidence angle and altitude are both clearly observable in the new LUTs. These data were generated at a constant 90deg azimuth angle. Color scale is in square kilometers for the entire DDMA region.



scattering area normalization of the DDMA, to arrive at NBRCS estimates of σ_0 . This has been corrected in Version 2.1 with an updated normalization area LUT which accounts for the changing altitude of the CYGNSS spacecraft.

After the calculation of the weighted DDMA sigma total as described above, $\sigma_{weighted}$, the bistatic scattering cross section is normalized as shown in Equation 8. In the Version 2.0 version of the calibration this was performed with a look-up-table which was a function of incidence angle and elevation angle only, at a constant altitude. This ignored the effects of the changing satellite altitudes and introduced (relatively) small errors (up to 0.1 dB) into the σ_0 estimation used in subsequent wind speed and MSS retrievals. In Version 2.1, a new LUT has been generated with an additional altitude dimension. This will allow the area normalization to correct for changes in the scattering area due to their slight eccentricity, as well as longer time scale orbit changes. An example sub-set of the new DDMA normalization areas (reduced to better reveal the changing LUT area magnitudes) is shown in Figure 10 as a function of incidence and altitude (at a constant azimuth angle). Testing of the new altitude dependent LUT has been validated to significantly reduce correlation of σ_0 with the satellite altitude.

Characterization of GPS Effective Isotropic Radiated Power (EIRP, v2.1 calibration)

The GPS Transmit Power, P_T and transmit antenna gain, G_T , or the effective isotropic radiated power (EIRP) can be estimated using a combination of ground based measurements and a parametrized model as a function of the transmitter space vehicle (SV) for all GPS satellites.

Transmit Power Estimation

A ground-based GPS constellation power monitor (GCPM) system has been designed, built, calibrated, and operated to measure the direct GPS L1 C/A signal [6]. The calibration subsystem and low noise amplifier (LNA) are implemented on a PID controlled thermal plate with extremely stable temperature control.

The measured GPS received power has been found to be highly repeatable, as tested for different satellites of three different block types. The measured EIRPs are verified by DLR/GSOCs independent measurements using a calibrated 30 m dish antenna with 50 dB L-band gain.

An optimization algorithm is used to estimate the transmit power of GPS L1 C/A-code by minimizing a cost function based on the difference between an engineering forward model prediction and the measurement of received power. We determine our best estimate of the GPS transmit power for L1 C/A signal by averaging 32 days of estimates of P_T , as given in Table I. More technical details of the GCPM system and the optimization algorithm can be found in [6].



PRN	$P_T(\text{dBW})$	Block	PRN	$P_T(\text{dBW})$	Block
1	15.09	IIF	17	16.39	IIR-M
2	13.79	IIR	18	14.04	IIR
3	14.77	IIF	19	13.66	IIR
4	-	-	20	13.48	IIR
5	16.28	IIR-M	21	14.43	IIR
6	15.38	IIF	22	14.39	IIR
7	16.86	IIR-M	23	15.41	IIR
8	15.42	IIF	24	15.03	IIF
9	15.49	IIF	25	15.32	IIF
10	16.28	IIF	26	15.22	IIF
11	13.67	IIR	27	15.34	IIF
12	16.88	IIR-M	28	14.27	IIR
13	13.89	IIR	29	16.84	IIR-M
14	13.20	IIR	30	15.47	IIF
15	16.08	IIR-M	31	16.35	IIR-M
16	13.93	IIR	32	15.87	IIF

TABLE I. Estimates of GPS Transmit Power (Level 1 C/A) for Version 2.1.

It should be noted that:

- 1) The estimated power values are indeed an “effective transmit power”, as the product of the exact transmit power and the transmit system gain correction factor (GCF).
- 2) The accuracy of the estimated power values are dependent on the accuracy of the baseline pattern (5th order power series of transmit antenna gain in [7]) used in the forward model simulation.

Transmit Antenna Gain Estimation

The transmit antenna directivity of IIR and IIR-M block type SVs has been published in [7], while that of IIF block type

SVs is unavailable to public. The baseline antenna pattern [8] used in the Level 1 calibration is a 5th order power series (polynomial fitting) of the azimuthally averaged published antenna pattern for IIR and IIR block and that of the averaged pattern of all 12 SVs using improved antenna panel (4 IIR and 8 IIR-M) for IIF block.

Discussion on GPS Transmitter EIRP Characterization

- 1) Transmit power and antenna pattern: The high resolution full transmit antenna pattern will be retrieved using the direct GPS signal measured by the CYGNSS zenith antenna, as discussed in [9]. Then the transmit power table will be further updated when the full patterns are applied to the optimization algorithm.
- 2) IIF block type power switching issue: 10 of the 12 IIF SVs switch the power sharing between the components in L1 over US east-coast and back over west-pacific in every orbit. It has been a stable behavior since the first quarter of 2017. Currently, the data measured by IIF block is flagged. This issue will be resolved by incorporating the CYGNSS zenith antenna measurement in Level 1 calibration.
- 3) SV retirement for PRN 18: On March 5th, 2018, SVN 54 (operating as PRN 18) retired. SVN 34 (Block IIA) is used for PRN 18 since March 20th, 2018. CYGNSS data using PRN 18 since then is



flagged.

- 4) Power redistribution for block IIR-M: A commanded redistribution of transmit power from M-code to C/A-code was performed for the 7 active IIR-M satellites on February 7 and February 8, 2017 [10]. The measured carrier-to-noise (C/N0) density ratio from different geodetic receivers experienced an approximately 1.5 dB-Hz increase on average. This phenomenon indicates an increase in the L1 C/A-code power for all 7 satellites after the maintenance was performed [11]. This event happened before the CYGNSS satellites were transitioned to science mode. No additional power redistribution for IIR-M satellites is reported since then.



Zenith EIRP Calibration (Version 3.0 calibration)

The v2.1 L1 calibration algorithm assumes a static value for the GPS transmit power and determines the GPS transmit antenna gain in the direction of the specular reflection point using an off-boresight azimuthal averaged estimate of the individual GPS transmitters. The GPS transmitter off-boresight antenna gains in the v2.1 CYGNSS calibration are based on publicly available pre-launch measured patterns provided by Lockheed-Martin. Additionally, release-controlled pre-launch pattern estimates for the Boeing Block IIF satellites were obtained and used to generate off-boresight gain look up tables for the GPS IIF satellites. For GPS transmitters without pre-launch patterns, an approximate pattern was estimated using the best available information.

Generally, these simplified one-dimensional GPS transmit antenna pattern approximations worked well enough to meet the low wind speed requirements. However, it suffers from a number of known problems which are addressed with the next version (v3.0) of the CYGNSS calibration algorithm, including,

- 1) The on-orbit GPS transmitter antenna patterns are known to contain differences from the pre-launch measured patterns, as the pre-launch measurements were not made while attached to the flight spacecraft bus. This most likely resulted in pattern distortions as the antenna interacted with the spacecraft and additional avionics present on the same face as the GPS transmit antenna, which were not considered when the pre-launch measurements were made.
- 2) It is generally understood that multiple GPS transmitters (notable the entire Block IIF satellites) operate using flexible transmit power levels. This occurs when the GPS operations center, without any announcement, will change the transmit power level of a GPS satellite for various but unknown reasons. This results in un-predictable jumps in the transmit power which are not accounted for in the v2.1 calibration algorithm, which assumes a constant transmit power level. These “flex-power” variations on the IIF block satellites necessitated the flagging out of all measurements from IIF satellite, greatly reducing the CYGNSS measurement coverage.

The v3.0 calibration algorithm is designed to greatly mitigate the above two error sources by estimating the GPS transmit power and antenna gain (Effective Isotropic Radiated Power, EIRP) using measurements from the direct (zenith) navigation channel of the CYGNSS delay Doppler mapping receiver (DDMI). By directly monitoring and linking the calibration to the direct observation of the GPS transmitter, the unpredictable flex-power changes can be detected instantly. Additionally, the new calibration technique requires only a ratio of the differences of the GPS EIRP between the direct and reflected instrument channels, resulting in lower uncertainties in the azimuthal asymmetries of the GPS transmit antenna patterns.

The (v3.0) Zenith EIRP Level 1 Calibration algorithm uses the same Level 1 calibration equation to calculate the delay Doppler Map bistatic radar cross section values (repeated below).

$$\bar{\sigma}(\hat{\tau}, \hat{f}) = \frac{P_g(\hat{\tau}, \hat{f})(4\pi)^3}{E'_S \lambda^2 G_S^R R_S^{Total}} \quad (11)$$



where, the two GPS transmitter terms are combined into a single term expressing the effective Isotropic Radiated Power (EIRP), consisting of the GPS transmitter power level and the GPS transmitter antenna gain in the direction of the specular point (SP), corrected by the ratio of receiver LNA gains. The combined GPS transmitter EIRP is expressed as,

$$E'_S = P_S^T G_S^T \quad (12)$$

The essential difference in the v3.0 calibration algorithm is that the GPS transmitter EIRP is estimated in real time using observations from the CYGNSS zenith navigation antenna, as opposed to using fixed look up table entries. The Zenith EIRP estimation used in the v3.0 calibration is described below.

Estimating the specular GPS EIRP using Zenith Navigation Signals

Estimating the GPS transmitter EIRP in the direction of the CYGNSS zenith antenna starts with the Friis equation for the received GPS power at the receiver,

$$P_Z = \frac{E_Z \lambda^2 G_Z}{(4\pi)^2 R_Z^2} \quad (13)$$

where, E_Z is the GPS transmitter EIRP toward the zenith CYGNSS antenna, G_Z is the CYGNSS zenith antenna gain, R_Z is the path distance from the GPS transmitter to the CYGNSS satellite. This expression can be rearranged to an expression for the GPS zenith EIRP (E_Z),

$$E_Z = \frac{(4\pi)^2 P_Z}{G_Z \lambda^2 L_Z} \quad (14)$$

Each of the terms in Equation 14 are calculated as,

- G_Z is estimated using the derived CYGNSS zenith antenna gain pattern over the full upper hemisphere of observation angles.

- L_Z is the range loss, calculated from the signal path as $L_Z = \frac{1}{R_Z^2}$, using the estimated CYGNSS receiver position (from its on-board navigation solution) and the GPS satellite position from the published IGS GPS ephemeris.

- P_Z is the estimated EIRP signal power at the CYGNSS receiver.

The raw power measurement of the zenith signal, $C_Z = I^2 + Q^2$ (in units of counts), is related to the signal power referenced to the input to the DMR by,

$$P_Z = 10^{0.1(a(C_Z, dB)^2 + b(C_Z, dB) + c)} \quad (15)$$



where C_Z , dB = $10\log_{10}(C_Z)$. The scaling quadratic regression coefficients (a,b,c) are derived from laboratory characterization tests of the EMulator, and P_z is in units of Watts. The default v3.0 zenith power conversion coefficients are shown in Table 1 below.

Coefficient	Value
a	0.011897122540965
b	-0.509944684931564
c	- 1.511603333176575e+02

Table 1, Zenith counts to power conversion coefficients

Subsequently, the EIRP of the GPS transmit signal in the direction of the CYGNSS specular point (E_s) can be related to the GPS EIRP in the direction of the zenith antenna (E_z) with two correction terms: a) the ratio of the analog LNA hardware gains between the two channels and b) a correction for the slightly different line of sight between the zenith and specular point directions. To facilitate this, new expressions for E_s and E_z can be used which include their respective LNA analog gains, such that,

$$E'_s = E_s A_s \quad (16)$$

$$E'_z = E_z A_z \quad (17)$$

In practice, the GPS EIRP towards the specular point can be calculated as a function of the LNA analog gain ratio and the ratio of the GPS EIRP values due to slightly different viewing geometry. Resulting in the following expression for the GPS EIRP towards the specular point,

$$E'_s = E'_z \frac{A_s}{A_z} \frac{E_s}{E_z} = E'_z [SZR_A][SZR_E] \quad (18)$$

Where,

- A_s/A_z is the ratio of the specular channel LNA analog gain and the zenith channel analog gain. Which is a function of CYGNSS FM and the specular (T_s) and zenith (T_z) LNA temperatures, respectively.
- E_s/E_z is the ratio of the specular channel GPS EIRP and the zenith channel EIRP, and is a function of the GPS transmitting Space Vehicle (SV) and the specular reflection incidence angle (theta).
- The SZR_A is the Specular to Zenith Ratio expression for A_s/A_z , which is a function of the CYGNSS observatory FM and LNA temperatures.



-The SZR_E is the Specular to Zenith Ratio for E_s/E_z , which is a function of the GPS transmitter and specular point incidence angle.

The specular-to-zenith EIRP ratio (SZR_E) is the azimuthally integrated ratio of the GPS transmit antenna gain in the direction of the zenith antenna to the gain in the direction of the specular reflection point, expressed as,

$$SZR_E(SV, \theta) = \int_0^{2\pi} \frac{G_Z^T(SV, \theta, \phi)}{G_S^T(SV, \theta, \phi)} d\phi \quad (19)$$

where phi is the azimuth coordinate of the GPS antenna gain pattern. The SZR ratio is a function of GPS SV number and of the incidence angle (theta) of the specular reflection point.

The ZSR_A is determined using the pre-launch characterized LNA gain vs temperature look-up-tables. The ZSR_E is estimated with empirically determined GPS transmitter antenna patterns, and converted to a look-up-table as a function of the specular point incidence angle for all GPS transmitters as a function of their SV number. For each measurement, the PRN number is converted to SV number from the latest available mapping of SV to PRN.

Finally, the estimated value of E'_s is substituted into the L1b calibration equation 1 and used to generate the v3.0 L1b BRCS DDM.

Rescaling of Nadir Antenna Patterns

Prior to launch, antenna pattern measurements were made for all of the port and starboard antennas. In addition, the predicted effects of the spacecraft body were extensively modeled using pattern simulation tools to attempt to accurately predict the final antenna patterns when attached to the spacecraft. These simulations included mechanical CAD models of the physical spacecraft with electromagnetic field simulations using the FEKO and Savant software packages. Additionally, full pattern measurements of the port and starboard antennas were made while mounted to a CYGNSS Engineering Model (EM) in an anechoic chamber. From the modeling effort, which was confirmed by the EM chamber measurements, we know that the solar panels have a significant impact on the observatory antenna gain patterns. The individual modeled pattern measurements were adjusted using a constant gain factor based on measured differences between the flight antennas to create the at-launch gain patterns for each CYGNSS flight model (FM) antenna calibration tables.

However, we know that there is potentially significant variability in the exact deployed positions of the solar panels from repeated pre-launch panel deployment tests. It therefore stands to reason that applying a simple constant offset for each of the FM antennas from the modeling and EM measurements is overly simplistic. It was evident from the initial analysis of the CYGNSS on-orbit data that an improved estimate of the CYGNSS antenna patterns was needed for each antenna in the constellation.

On-orbit estimates of $\sigma_{0,anom}$ described above have been calculated for all CYGNSS flight antennas. For each flight antenna in the constellation (1 port and 1 starboard antennas for each of 8 spacecraft = 16 total antennas), $\sigma_{0,anom}$ anomalies were computed in 1 degree increments of spacecraft off-nadir and azimuth angle. These antenna correction maps were then smoothed over 5 degree windows in azimuth and off-nadir angle in order to reduce measurement noise. These results were then interpolated



using nearest neighbor interpolation to a resolution of 0.1 degree. This map of $\sigma_{0,anom}$ as a function of antenna coordinates was used to scale the original patterns to produce a new estimate of the receive pattern gain, which greatly reduced the observed azimuthal anomalies (anomaly subtracted from original antenna pattern in logarithmic space from estimates of gain in dB). This was done for all 16 operational flight antennas on all 8 observatories for Version 2.1.

The resulting $\sigma_{0,anom}$ anomalies gain maps as a function of azimuth averaged across all 8 spacecraft is shown in Figure 11. The anomalies, which were initially greater than as 40% are reduced to less than 20% residual anomalies across all azimuth angles. The regions near the azimuth angles where most measurements are taken (90 and 270 degrees for Starboard and Port, respectively) have errors reduced to 10% or less. The remaining errors are most likely due to variability within the data not related to wind speed, incidence angle, or receiver antenna pattern effect accounted for in this analysis.

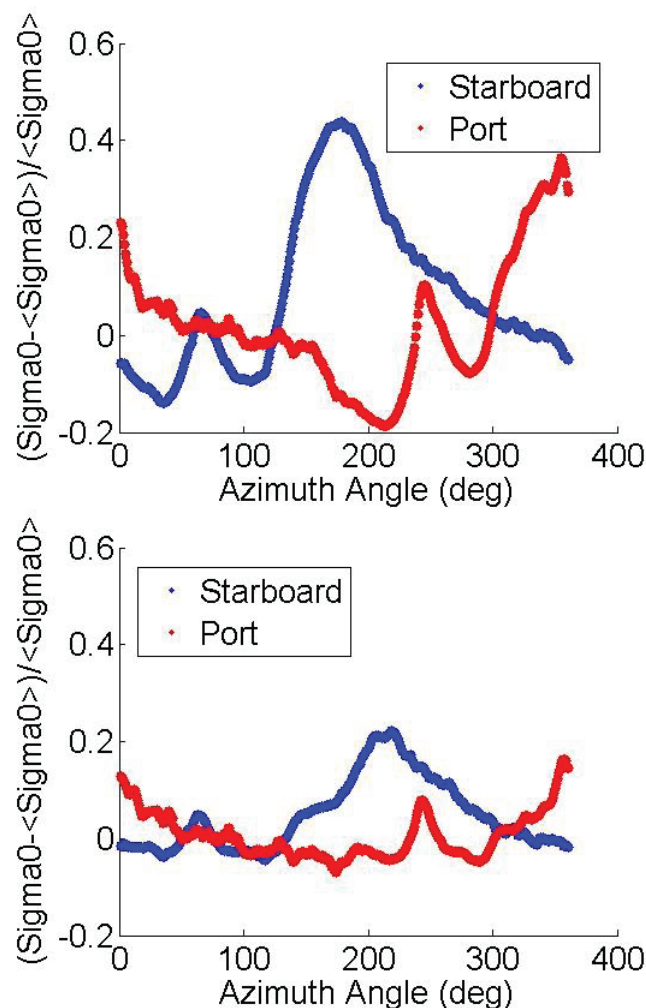


Fig. 11. (above) σ_0 anomalies computed for Level 1 data between day of year 77 and 121 of 2017 on the Version 1 using pre-launch estimated receive antenna patterns. (below) σ_0 anomalies computed for Level 1 Corrected data for Version 2 of the L1 calibration. The anomalies reduce the worst case error of 40% to less than 10%.

It should also be noted that off-nadir angle is highly correlated to incidence angle for a given spacecraft orientation, with the relationship directly tied to the spacecraft roll, which changes periodically as the spacecraft are adjusted to maintain a power positive orientation for high solar beta angles.

As noted above, Version 2.1 of the CYGNSS data includes a rescaling of the at-launch assumed zenith antenna patterns based on matchups of CYGNSS derived L2 winds with model-based matchups. These



L2 estimates are based on empirically derived geophysical model functions connecting L1 normalized bi-static radar cross-section (NBRCS) estimates that are themselves based upon the antenna patterns and model-based matchups themselves. In order to place the antenna pattern rescaling on a more physically sound basis, the Version 3 antenna patterns were rescaled using matchups with model-based estimates of MSS.

The relationship between MSS as a function of incidence angle θ is given by:

$$\text{NBRCS}(\theta) = \frac{|R|^2}{\text{MSS}} \quad (20)$$



Where R is the Fresnel coefficient evaluated at θ . For the version 3 antenna pattern rescaling, matchups between IFREMER WaveWatch III (WW3) estimates of MSS and CYGNSS data were created for all data in 2019 with the CYGNSS data filtered by the overall Level 1 quality control flag. In order to match the wave spectra of CYGNSS derived MSS, the tail of the IFREMER MSS spectra were extended assuming an Elfouhaily wave spectrum. With this extended WW3 MSS, a model based NBRCS was computed using Equation 20. For each CYGNSS, WW3 MSS matchup, the mean ratio of the observed to model NBRCS was computed in 1 degree bins of antenna elevation and azimuth angle for all 16 CYGNSS nadir antennas (port and starboard antennas of all 8 satellites) within a range modelled NBRCS of 30-40, which contains 20% of the observed data while focusing on the peak of the NBRCS distribution (Figure 12). The distribution of the ratio of observed to model NBRCS for 2019 data is shown in Figure 13. This ratio has mode of 0.5, leading to a resulting rescaling of the antenna patterns of around 3 dB (e.g., Figure 14). A comparison of model and retrieved NBRCS before and after rescaling is shown in Figure 15. A comparison of the model and CYGNSS MSS after rescaling is shown in Figure 16. In addition to producing MSS estimates that agree much more with model estimates, the antenna pattern rescaling also results in NBRCS estimates that vary less from antenna to antenna as shown in Figure 17.

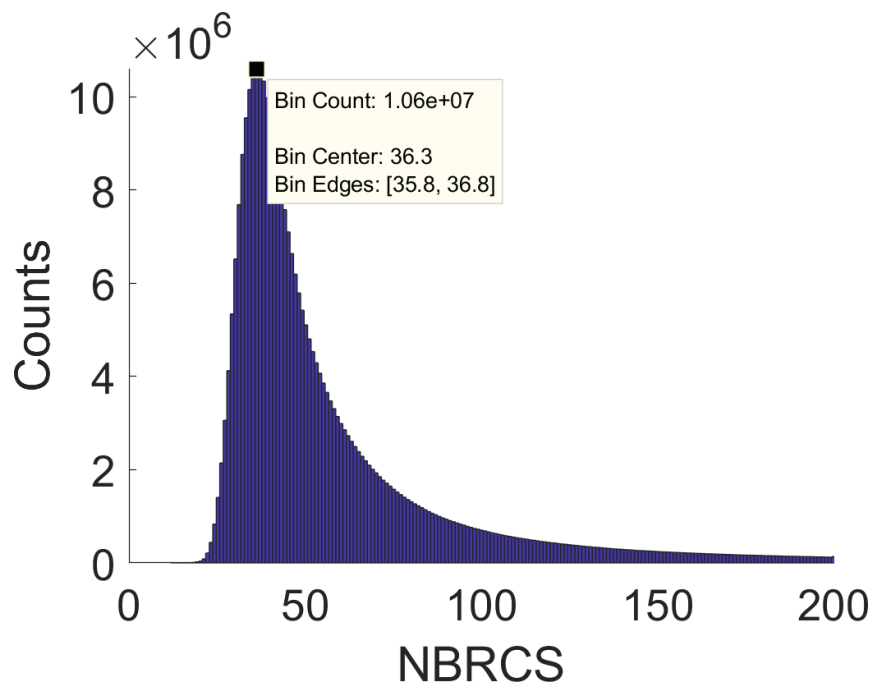


Figure 12. Distribution of model based NBRCS from WW3 data for 2019.

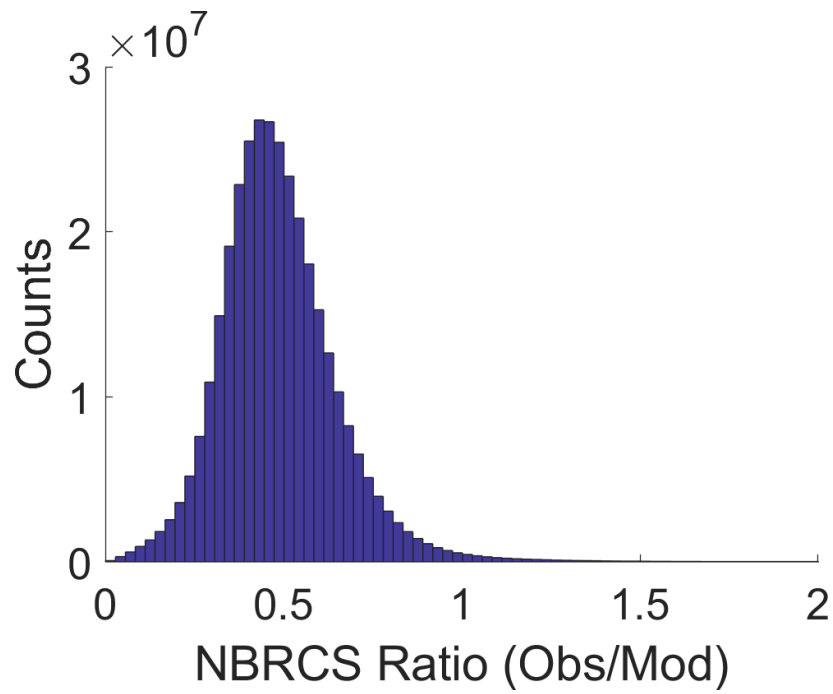


Figure 13. Distribution of ratio of observed to model based NBRCS for 2019 data.

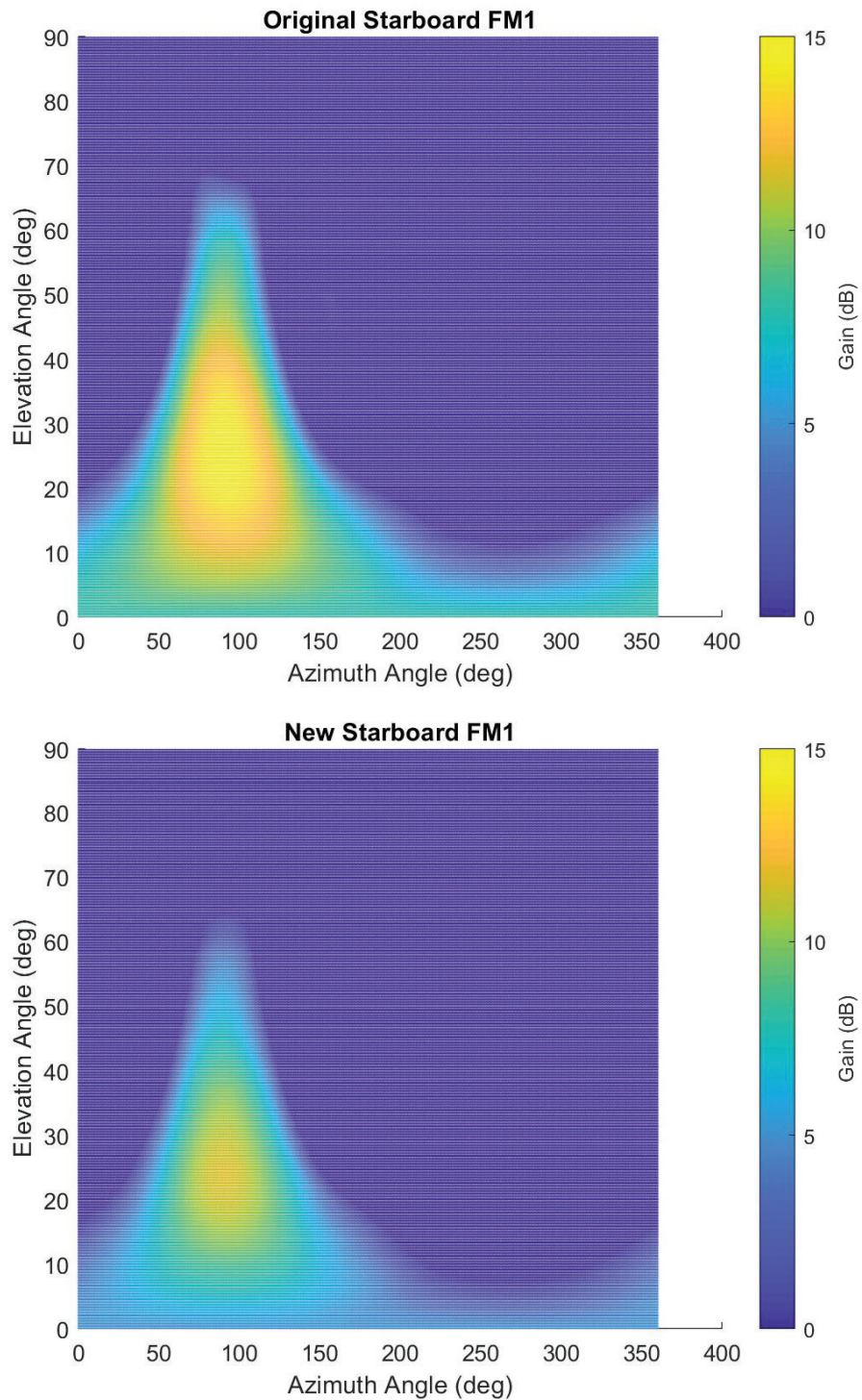


Figure 14. Original (top) and updated (bottom) antenna patterns for CYGNSS satellite 1 starboard antenna. Other antenna pattern rescaling are similar. Peak gains were reduced by about 3 dB.

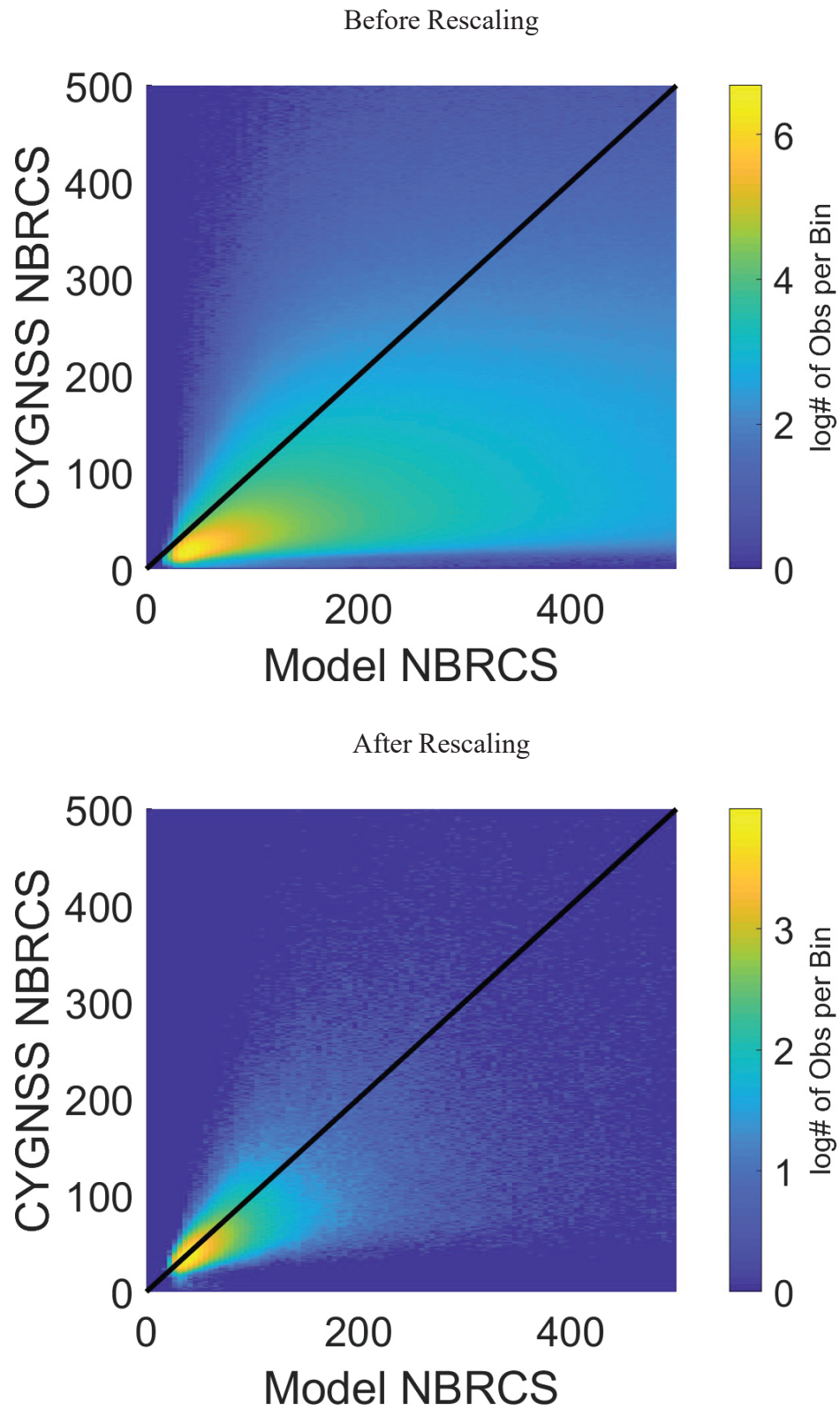


Figure 15. Comparison of model based and CYGNSS NBRCS before (top) and after (bottom) antenna pattern rescaling.

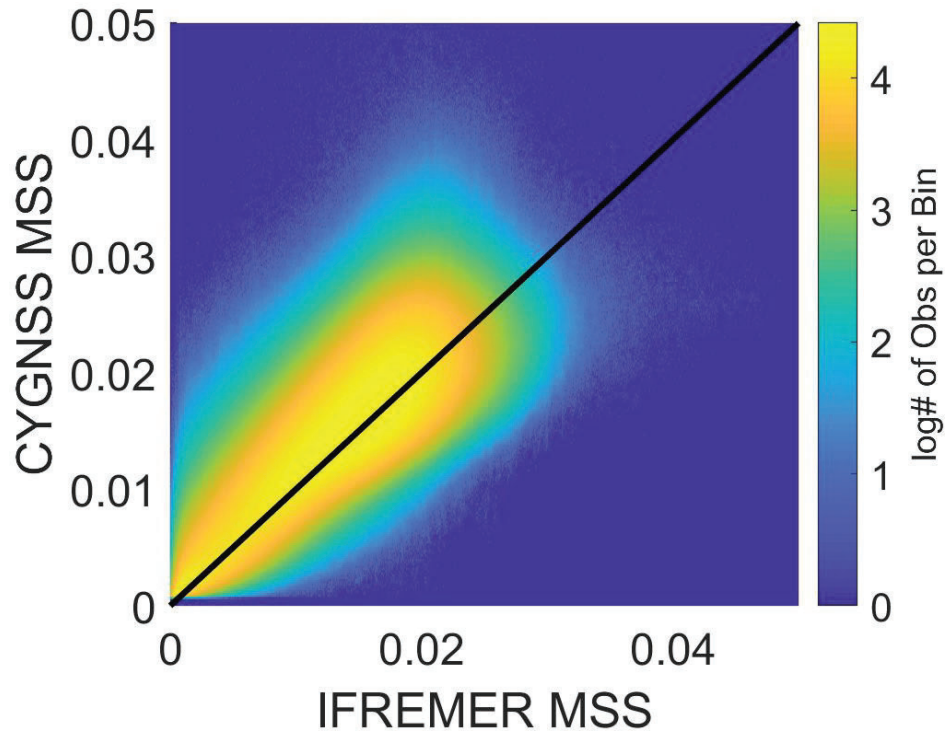
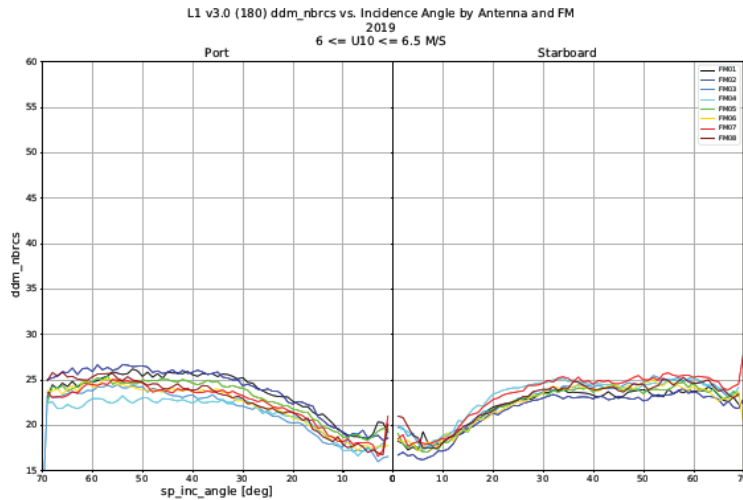


Figure 16. Comparison of model and CYGNSS MSS before (top) and after rescaling.



Before Rescaling



After Rescaling

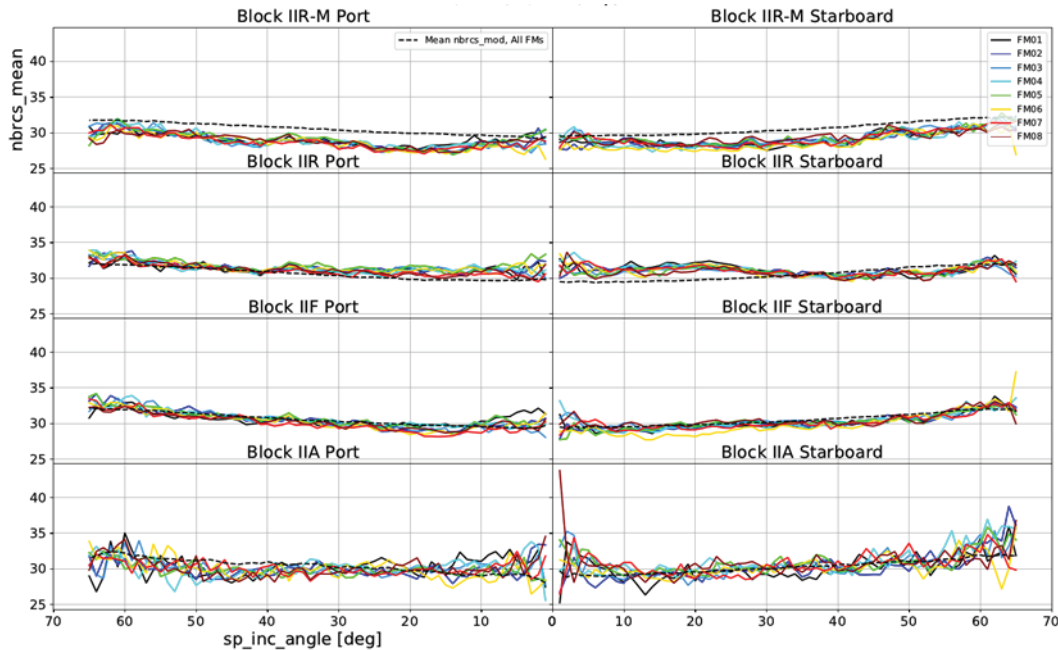


Figure 17. Mean NBRCS as a function of incidence angle for the starboard and port antennas of each FM before (top) and after (bottom) antenna pattern rescaling.

NBRCS and EIRP Normalization

In addition to rescaling the nadir antenna patterns, comparisons of the CYGNSS observed NBRCS as a function of transmitter (GPS SV) and receiver (CYGNSS antenna and FM) to the model based NBRCS demonstrated significant variability from SV to SV and FM to FM for not just the NBRCS, but also the SV dependent EIRP going into the calculation of NBRCS. For this reason, normalization of the EIRP and NBRCS is completed prior to their use in computing the observed NBRCS.



For the NBRCS normalization, a significant dependence of the NBRCS upon incidence angle that varied from receiver to receiver and SV to SV was noted in the data. Due to this, the computed NBRCS are normalized by SV, FM, antenna (starboard, port) and incidence angle in 1 degree increments for all data at the given SV, FM, antenna, and incidence angle set from the data from 2019.

On February 14 of 2020, the flex power mode for the GPS constellation changed significantly, such that the EIRP of the II-RM block satellites shifts noticeably relative to data prior to this data. Because of this, the EIRP for the II-RM SVs is rescaled to match that of the data prior to this change to avoid a discontinuity in CYGNSS NBRCS at that date. This was achieved by normalizing the post Feb 14, 2020 data to the pre-change data by the ratio of the mean of all block II-RM NBRCS data pre- and post-changed.

Figure 17 above shows the comparison of modelled and observed NBRCS with these changes. Figure 18 shows the mean NBRCS histograms by FM after normalization. Figure 19 shows histograms of NBRCS broken out by block type before and after these normalizations.

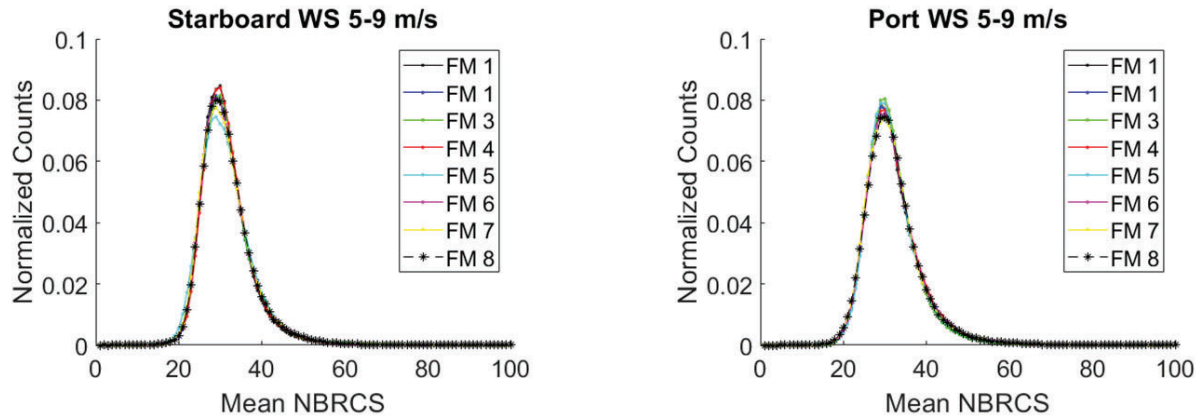


Fig. 18. Mean NBRCS histograms by FM for winds between 5 and 9 m/s for starboard (left) and port (right) antennas

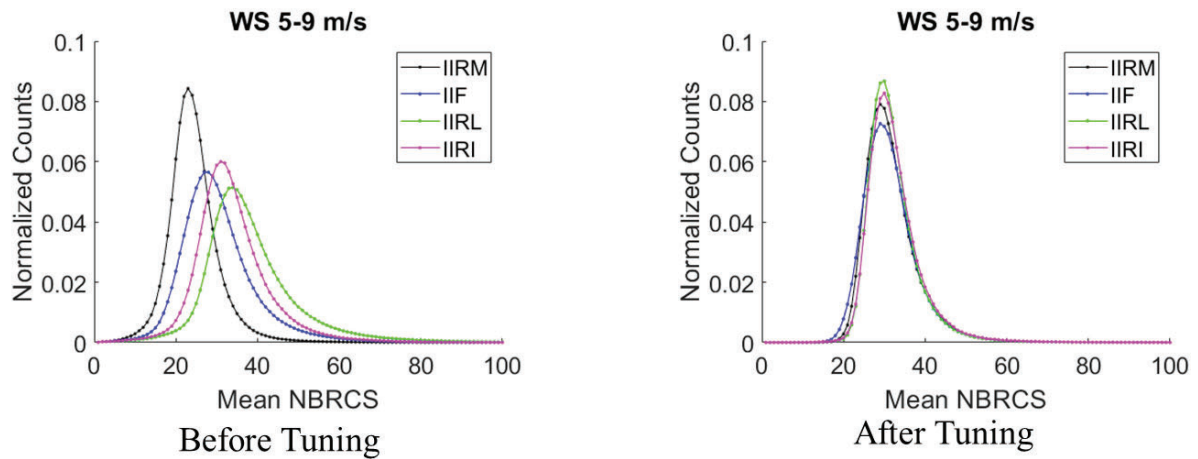


Fig. 19. Mean NBRCS histograms by GPS block type for winds between 5 and 9 m/s before (left) and after normalization.

CYGNSS LEVEL 1 ERROR ESTIMATION METHOD

This analysis assumes that the uncertainties in the CYGNSS Level 1 calibration algorithm are generally independent uncorrelated error sources, which can be characterized with a zero mean Gaussian distribution. This may not be strictly the case for some terms (most notably the GPS transmit power levels), yet to a first order this analysis serves to bound the expected error and as shown in the top-down



analysis in Ruf et al [12] is consistent with the best estimate of the overall on-orbit observed CYGNSS wind retrieval performance. The method for this error analysis is based on the partial derivative method presented in Jansen et. al [13]. Additionally, the rolled up error was simulated using a Monte Carlo simulation and was in agreement with the partial derivative estimated error levels presented below.

For more details on the partial derivatives for individual error terms in the L1a and L1b calibration equations refer to Gleason et al [5].

Error Analysis Methodology

The total error in the L1a or L1b calibrated DDM is the root of sum of squares (RSS) of the individual errors sources in the independent terms of their respective expressions, which can be expressed generically as,

$$\Delta L_1^{a,b} = \left[\sum_{i=1}^x [E(q_i)]^2 \right]^{1/2} \quad (21)$$

where $L_1^{a,b}$ are the L1a and L1b estimated error values, x is the number of independent errors terms and q_i are the respective input error parameters. The individual errors terms can be estimated by taking the partial derivatives of the calibration equation such that each error term in the process can be quantized as,

$$E(q_i) = \left| \frac{\partial L_1^{a,b}}{\partial q_i} \right| \Delta q_i \quad (22)$$

Rolled Up On-Orbit Level 1 Calibration Errors

The wrapped up errors of the Level 1b calibration can be expressed in a similar manner, with the total L1a error rolled in, and estimated over the DDMA region of the DDM (3 delays x 5 Dopplers),

$$\bar{\sigma}_{DDMA}^0 = \frac{P_{g,DDMA} (4\pi)^3 L_{atm}}{P^T \lambda^2 G_{SP}^T G_{SP}^R R_{SP}^{Total} A_{DDMA}} \quad (23)$$

Substituting this equation into Equation 22 results in,

$$E(q_i) = \left| \frac{\partial \bar{\sigma}_{DDMA}^0}{\partial q_i} \right| \Delta q_i \quad (24)$$



Where the errors terms are: $q_1 = P_g$ (rolled up L1a errors), $q_2 = DDMA_{crop}$, $q_3 = L_{atm}$, $q_3 = R_{SP}^{Total}$, $q_4 = P_T$, $q_5 = G^T$, $q_6 = G^R$ and $q_7 = A$, respectively.

The On-orbit estimated Level 1 calibration errors 1-sigma estimates are shown below for each input parameter as well as explanations for each term.

Error Term	Error Magnitude (at 10 m/s reference wind)	Comment
E(Pg)	0.23 dB	Rolled Up L1a Error [14]
E(DDMA)	0.1 dB	Error in DDMA Weighting Algorithm
E(R_total)	0.01 dB	Based on total range error estimates of 2000m (very conservative)
E(EIRP)	0.32 dB	GPS Transmitter EIRP error
E(GR)	0.43 dB	Estimated Receiver Antenna Gain Error From MC Simulation
E(A)	0.05 dB	Effective Scattering Area Error, From E2ES

TABLE II. Level 1B input parameter error estimates.

- 1) E(Pg) is the rolled up L1a error from [5].
- 2) E(DDMAcrop) is an estimate of the error in the DDMA Weighting algorithm detailed above. The weighting algorithm uses a linear interpolation over non-linear DDM bins and this will introduces some error in the cropping of the final value. The value of 0.1 dB is an approximation based on ideal simulations of the DDMA weighting algorithm.
- 3) E(R Total) is the total error due to mis-estimation of the path loss from the GPS transmitter to the specular point to the receiver. Given the relatively high accuracies of all three of these parameters, this error is expected to be negligible. More details on the contribution due to the single frequency GPS receiver position estimation performed on CYGNSS can be found in [15].
- 4) E(EIRP) = E(PT) + E(GT) is the error in the GPS transmit power and antenna gain correction. The best estimate for this error is based on the top down analysis reported in [24].
- 6) E(GR) is the error in the receive antenna gain and is based on the analysis of σ_0 anomalies described above, after the described corrections to the receive antenna patterns were applied. The antenna gain error was estimated using Monte Carlo simulations based on the predicted statistical spacecraft attitude performance and best estimate of the receive antenna gain pattern, described in more detail in [5].
- 7) E(A) is the estimated error in the effective scattering normalization area used to convert σ to σ_0 . The CYGNSS End-to-End Simulator was used to generate the look-up-tables used to generate these values. Given the extensive validation of the E2ES this error was at a relatively low value, driven by errors introduces due to the integration step size used in the table generation, plus a small amount of margin.

Rolled up L1 Uncertainty

The rolled up L1 error budget is a function of multiple terms all of which it is impractical to include



in a per observation look up table. For this reason the L1 uncertainty included with each L1 sigma0 estimate in the CYGNSS official products is considered only for the two most influential variables; the magnitude of the sigma0 itself and the range corrected gain at each observation (which wraps up both the receive antenna gain and range losses). As can be seen from Equations 23 and 24 (and derived in greater detail in [5]), the partial derivative contributions weight the error magnitudes differently based on the observation parameter inputs. The largest scaling factor is the overall received power, which scales directly with the surface sigma0 and the receive antenna gain and path losses. Other variables which impact the received power or otherwise weight the error terms are not considered for simplicity and as they are generally lower order than the changes induced by the surface conditions and receive antenna gain. The resulting rolled up L1 errors for three example sigma0 reference values and over a full range of RCG is shown in Figure 20 below.

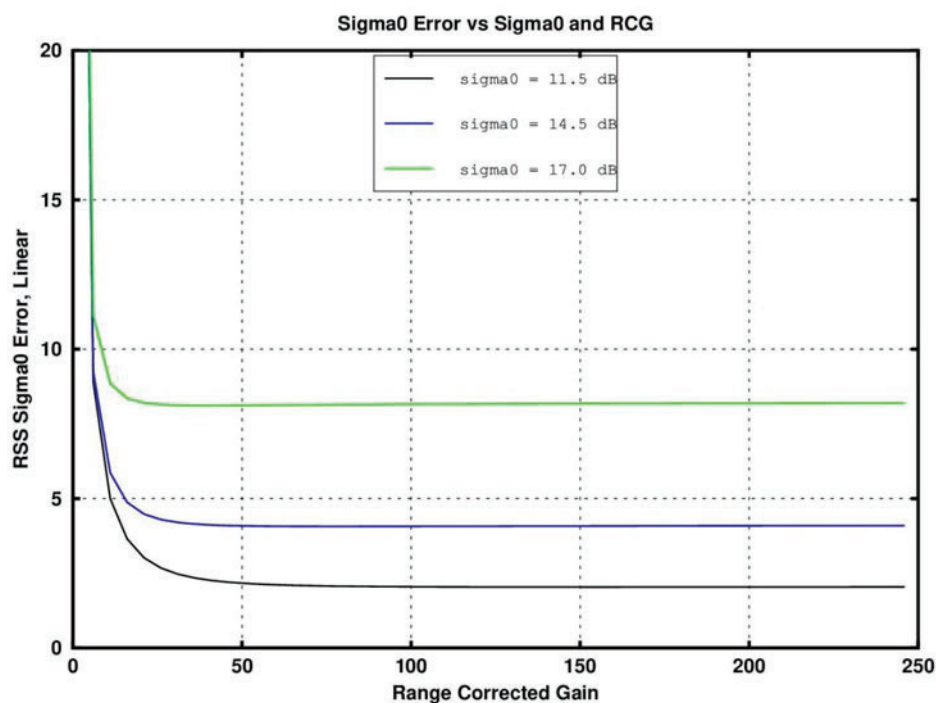


Figure 20. Level 1 sigma0 uncertainty at three reference sigma0 levels and over a full range of received RCG. These corrections correspond to roughly 13% of the reference sigma0 at the typical (greater than 50) values of RCG.

CYGNSS Level 1 Bin Ratio Correction

CYGNSS Analog to Digital Convertor (ADC) Design

A full explanation of the CYGNSS analog to digital sampling configuration and calibration corrections can be found in Gleason et al 2021 [17].

The CYGNSS instrument input signal processing chain includes the following steps: After capturing the off-air signal by the receive antenna, the signal enters the low noise amplifier (LNA) and is processed through a cavity filter and initial fixed voltage gain stage. Following this initial amplification stage, the received signal travels to the instrument front end where additional down-conversion and filtering is applied. This includes added amplification by a commandable voltage gain which permits adjustment of the analog signal level into the ADC. It is noted, that numerous GPS receivers configure



the front end into an Automatic Gain Control (AGC) mode in order to autonomously adjust this variable gain stage, thereby securing an ideal Normal sampling distribution. However, the need for knowledge of the precise input power level for a science observation prohibits this convenience on the CYGNSS instruments, and necessitates that the commandable gain stage remains at a constant commanded value for the CYGNSS receivers.

The need to manually command the front end gain settings, adds the requirement that the input signal levels be compatible with the 2-bit ADC digital sampling thresholds (which are fixed within the front end). When the gain is set too high (increased magnitude of real analog voltage samples), the sampled input signal falls disproportionately into the outer sampled bins which results in a non-ideal inverted sampling distribution as shown directly below.

Alternatively, if the commanded gain is too low the sampling shifts to the (lower voltage) inner two bins of the 2-bit sampling and results in a peaked sampling distribution. The optimal configuration is when the gain is commanded to a level which results in a near-ideal Normal (Gaussian) sampling distribution over the 4 digital sampled bins.

As the sampling distribution deviates from the Normal (Gaussian) shape, a small and gradual degradation in the downstream processed retrieved signal power levels arises [18]. It is important to note that GNSS signals when sampled off-air are typically at levels well below the input noise floor and are subsequently detected using a coherent (spread spectrum) processing technique in the digital signal processor such that the sampling distribution in a GNSS receiver is driven mostly by the input noise level [19].

It is convenient to define a single metric to quantify the digital sampling distribution. We have chosen to do this in a parameter called the Bin Ratio (BR), which is defined as,

$$BR=(b_2+b_3)/(b_1+b_4)$$

(25)

where, b_1 , b_2 , b_3 , b_4 are, respectively, the number of counts accumulated into each of the four digital sampling bins, -3, -1, +1 and +3 respectively over a short time interval that in the case of the CYGNSS receivers is 1 second.

Impact of On-Orbit Bin Ratio Fluctuations on L1 Calibration

To demonstrate the impact of fluctuating bin ratio on the primary CYGNSS level 1 (NBRCS) and Level 2 (wind speed) products, a 1-year long CYGNSS data record was analyzed across all observatories for both port and starboard science channels.

Figure 1 illustrates the positive correlation of NBRCS and BR over a full year year of CYGNSS data (2019). Bin ratio estimates over this year long data record are computed using Equation 1 and the NBRCS is the mean value across all CYGNSS observatories within narrow (0.05 width) bins. The surface MSS and wind speed reference data are based on temporal and spatial match-ups from ECMWF ocean surface wind speed (in 0.25 m/s bins). The estimated uncertainty in the ECMWF winds



has been estimated to be on order of 0.5 m/s RMSE [20]. Additionally, WaveWatch III (WW3) wave mean square slope model [21] has been used as a surface reference. To account for the CYGNSS observation frequency, an L-band adjusted spectral tail [22] has been applied to the WW3 outputs and the surface isolated over narrow MSS conditions (in 0.0005 width bins). The accuracy of this L-band spectral tail corrected model MSS is unknown and the subject of on-going research. Yet, these data provide a more direct surface link to the CYGNSS L-band observations than the near surface wind speeds and are included as a secondary comparison source.

In the idealized scenario of no calibration errors or uncertainties, NBRCS estimates should be independent of all instrument quantities with no correlation to bin ratios. The clear correlation of NBRCS on BR and how this may compromise the accuracy of the constellation's level 1 calibration if not accounted for in the CYGNSS wind speed estimation algorithms that rely on NBRCS in their retrievals. Figure 21 demonstrates the need for a digital sampling correction based on the observed BR.

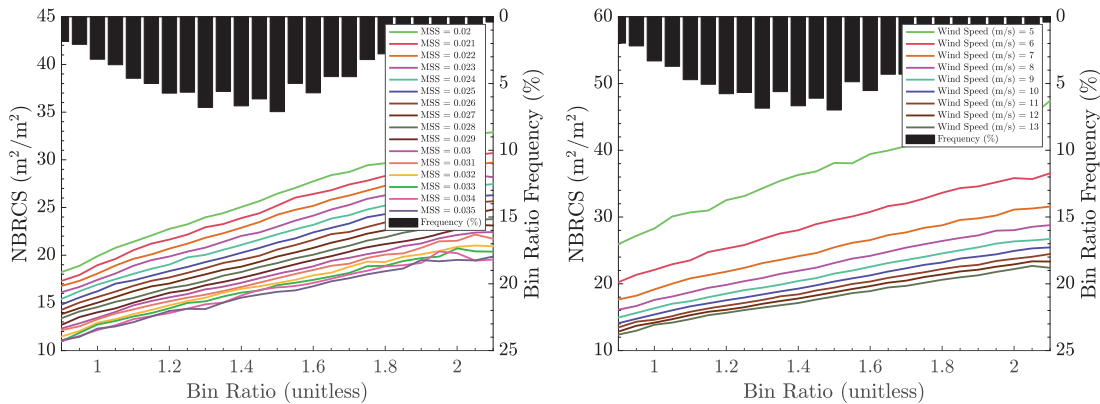


Figure 21. Mean NBRCS estimates vs science channel bin ratio for a wide range of ocean conditions without digital sampling correction. (Left) Over a range of surface MSS conditions (ref. WW3) and (Right) over a range of wind conditions (ref. ECMWF)

Nadir Bin Ratio Correction

The input noise power is the dominant component of the pre-correlated GPS signal received at the instrument ADC converter. Thus, a correction to the observed noise floor can be performed to mitigate received power uncertainty due to BR fluctuations driven largely by external noise variations. The correction is designed as an adjustment to the per-observation estimated CYGNSS level 0 noise counts. The received signal power counts in the CYGNSS level 1 calibration are estimated after subtraction of the estimated noise floor; that is the difference of the total counts and noise counts. As a result, by correcting the noise counts, we are directly adjusting the downstream estimated level 1 power levels, including the normalized bistatic cross section (NBRCS) estimate.

The noise floor correction was derived using a theoretical simulation of the CYGNSS hardware configuration as detailed in [1]. Upon application of the theoretical correction it was observed that the results could be improved slightly by adding a modest multiplicative scaling factor to the theoretical correction. The final nadir channel noise floor corrections applied to the CYGNSS Level 1 data is the empirical correction curve shown in Figure 22. The noise floor correction vs BR is stored in a look up table (LUT) and applied to every CYGNSS level 1 observation based on the BR calculated as in



Equation 25 and the empirical correction LUT as shown in Figure 22.

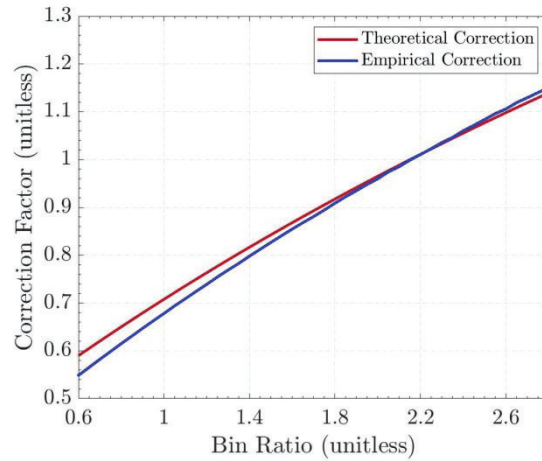


Figure 22. Theoretical and empirically adjusted digital sampling noise floor corrections applied to CYGNSS v3.1 level 0 noise levels.

The post-correction NBRCS vs BR performance is shown in Figure 23 across ranges of MSS and wind speed bins. A summary of the results of this analysis is included in Table 1. These statistics are generated using all CYGNSS data from 2019, with temporal and spatial co-locations data from ECMWF (U10 wind speed) and WaveWatch III (L-band corrected MSS) used as the validation reference dataset.

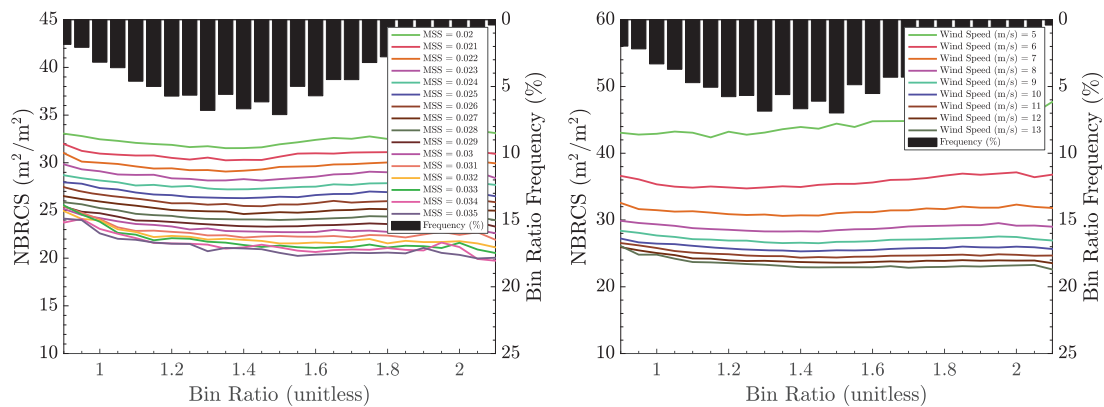


Figure 23. NBRCS estimates vs science channel bin ratio over a range of ocean conditions with noise floor correction. (Left) With respect to surface MSS conditions (ref. WW3) and (Right) over a range of near surface wind conditions (ref. ECMWF).



Surface Conditions	NBRCS RMSD (linear)	NBRCS Slope ($(\Delta\text{NBRCS}/\Delta\text{BR})$)	NBRCS RMSD (linear)	NBRCS Slope ($(\Delta\text{NBRCS}/\Delta\text{BR})$)
Uncorrected				
Corrected				
Wind Total (5-20 m/s)	12.90	9.34	2.79	1.48
Low Winds (5-7 m/s)	19.50	13.91	4.19	2.24
Medium Winds (7-12 m/s)	13.75	9.90	1.60	0.38
High Winds (12-20 m/s)	10.64	7.80	3.11	1.93
MSS Total (0.020-0.025)	12.86	9.30	1.89	0.84
Low MSS (0.020-0.025)	15.04	10.80	2.06	0.99
Medium MSS (0.025-0.030)	12.59	9.09	1.35	0.26
High MSS (0.030-0.035)	10.93	7.99	2.19	1.19

Table 1. Summary of CYGNSS pre-correction and post-correction NBRCS root mean square deviations across wind speed (ref. ECMWF) and MSS (ref. WW3) surface conditions.

Zenith Bin Ratio Correction

The CYGNSS zenith observations consist of integrated signal plus noise counts only, without a reference noise floor. This prohibits the application of the nadir noise floor correction to the zenith channel observations. Therefore, the observed zenith signal plus noise counts need to be corrected directly before a real-time EIRP estimate is formed [23]. Note that a decrease in the noise floor in the nadir calibration is equivalent to an opposite adjustment to the total signal plus noise counts.

Like the nadir digital sampling correction, the zenith correction can also be optimized using empirical tuning factor(s) to ensure consistency of the EIRP estimation as a function of natural bin ratio fluctuations. Due largely to the spread of zenith bin ratio PDFs with means under that associated with an ideal Gaussian distribution, applying a single correction across all zenith observations was not possible and individual per-observatory corrections are required.

The per-FM zenith digital correction functions are shown in Figure 24. To better illustrate the need for an increased empirical correction factor as the mean BR of the distributions decreases, the per-FM corrections are shown only between their 5% and 95% bin ratio limits, to better illustrate the correction values where the on-orbit observations occur for each CYGNSS FM. As a given zenith bin ratio distribution approaches that of an ideal Gaussian distribution, only modest empirical adjustments are needed. For example see the CYG05 correction in Figure 24. In contrast, as the bin ratio distribution diverges from this ideal reference PDF, a need for significantly increasing the correction ‘weights’ at a



given bin ratio is evident. An example of this is CYG04 which requires a much larger empirical scale factor.

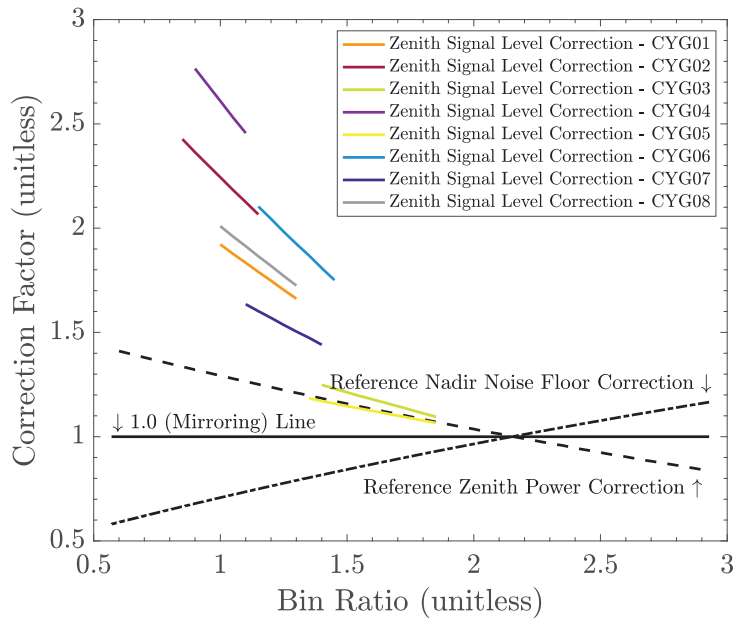


Figure 24. CYGNSS FM specific zenith digital correction functions. Reference nadir correction is flipped around the 1.0 axis to accommodate the opposite signal plus noise counts correction. Scale factors are derived and applied to each FM individually. Corrections are shown for each FM over the 5%-95% range of observations where they are applied. This clearly demonstrates the deviation from the reference correction as the BR distribution shifts downward.

The zenith signal digital corrections are evaluated with respect to the consistency of EIRP estimation across BR by each CYGNSS FM. An example of the before and after correction EIRP estimation across BR for CYGNSS FM 3 is shown in Figure 25. Before the digital sampling correction is applied there is a clear positive linear trend in the EIRP over a large range of BR (the bin ratio limits over which 95% of data occurs for a given FM). After the correction is applied the EIRP estimation is significantly more consistent (i.e. flatter) over the same BR range, reducing the maximum EIRP slopes by ~92%. The pre-correction and post-correction estimated EIRP root-mean-square-difference (RMSD) presented on a per-FM basis are listed in Table 2.

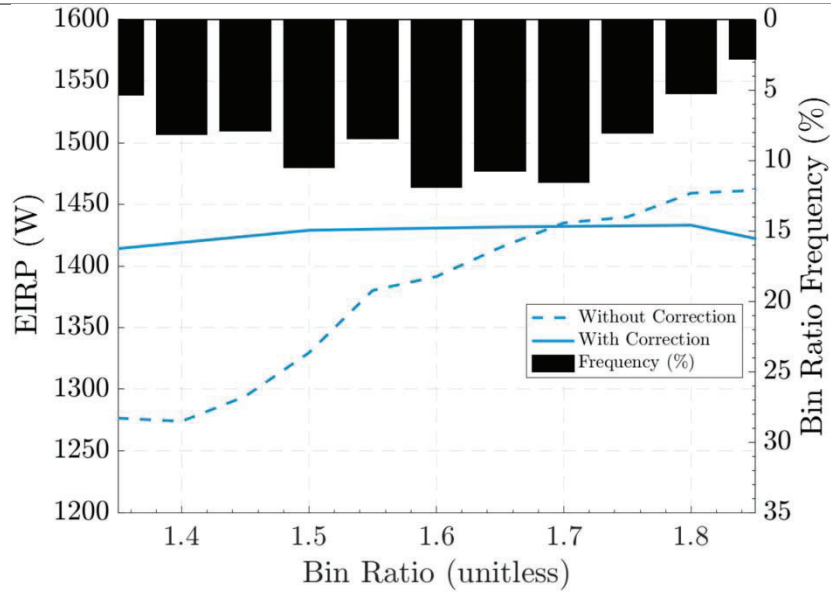


Figure 25. Example zenith mean EIRP estimation over the BR range containing 95% of zenith observations for CYGNSS FM5. The pre-correction estimates (dotted line) clearly show a positive trend with BR that is largely mitigated with the digital sampling correction (solid line).

Parameter	FM 1	FM 2	FM 3	FM 4	FM 5	FM 6	FM 7	FM 8
Empirical Scale Factor, Y(FM)	3.15	4.25	1.35	5.50	0.93	4.40	2.40	3.45
Zenith BR Mean	1.17	0.99	1.64	1.01	1.64	1.35	1.25	1.16
EIRP RMSD, Uncorrected	113.97	123.88	96.76	101.19	72.69	130.30	101.17	102.85
EIRP RMSD, Corrected	23.91	28.99	20.91	16.18	22.83	23.40	24.21	19.57

Table 2. Summary of CYGNSS zenith channel bin ratio distributions and EIRP pre-correction and post-correction performance.

DDMA normalization area re-scaling

Using the CYGNSS End-to-End simulator, estimates of the physical scattering areas (5) and subsequently the effective scattering areas (6) under varying observation geometries are derived and used to generate a reference A_{tot} LUT for use in the normalization of DDMA radar cross section (8) estimates. An example of this is shown in Figure 6 where surface delay-Doppler solutions are developed on a high resolution (50 meter) grid and subsequently used to identify surface grid pixels corresponding to a given delay τ - Doppler f pair.

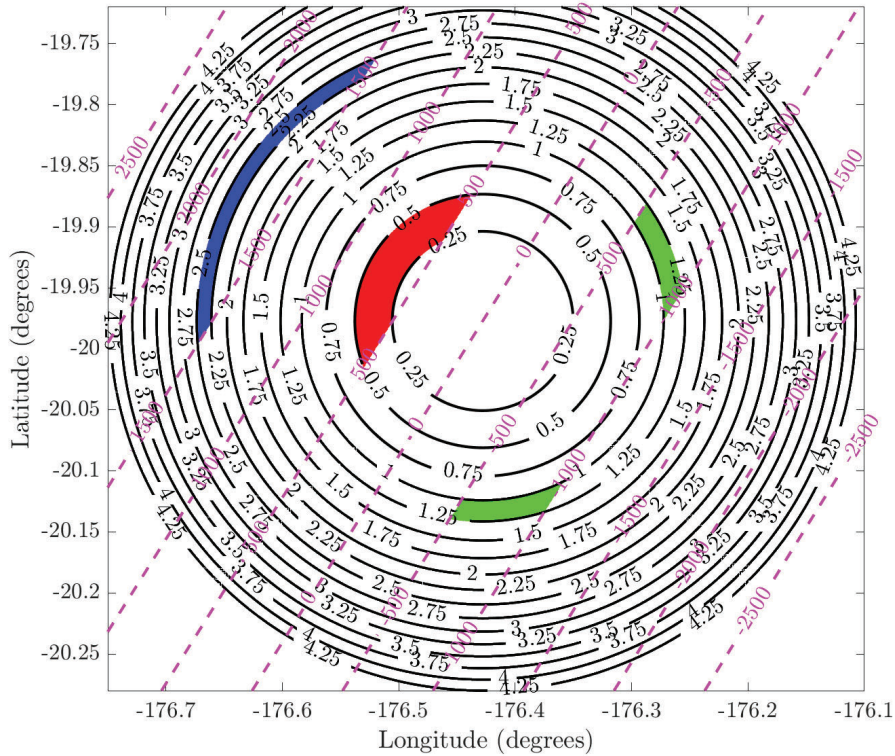


Figure 26. Example of surface grid used to develop physical scattering area DDMs. Iso-delay (Chips) lines are in black, iso-Doppler (Hz) lines are in magenta. For illustrative purposes, the physical area using a **forward binning scheme** corresponding to $A(\tau = 0.25 \text{ chips}, f = 500 \text{ Hz})$ is in red, $A(\tau = 1 \text{ chips}, f = 1000 \text{ Hz})$ is in green and $A(\tau = 2.25 \text{ chips}, f = 1500 \text{ Hz})$ is in blue.

It is noted that the determination of the relevant areas is limited to resolutions of ~ 0.25 chips and ~ 500 Hz to match the delay Δ_τ Doppler Δ_f resolutions of the Level-1 DDM. The original scattering area estimates were based on a forward binning scheme where the physical scattering area at delay τ and Doppler f comprises the footprint spanning $\in [\tau + \Delta_\tau, f + \Delta_f]$. It follows that the maximum delay/Doppler binning errors associated with the estimation of the physical area (5) are comparable to Δ_τ and Δ_f , respectively.

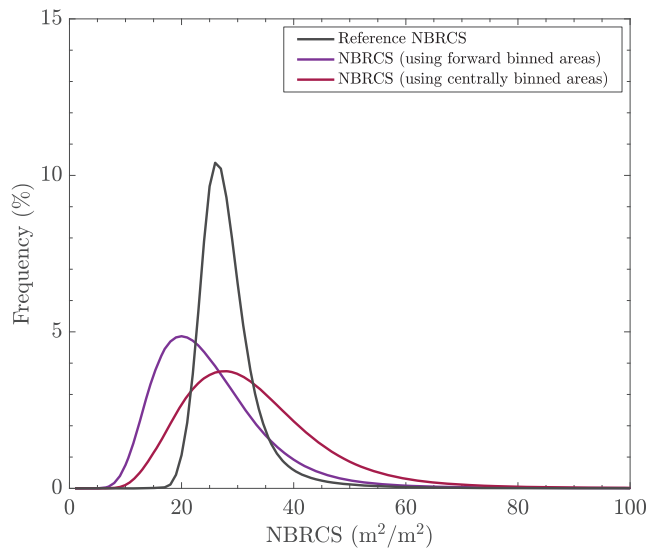




Figure 27. NBRCS PDFs summarizing the effects of revised DDMA normalization area estimates. An example of how this may compromise normalized radar cross section estimates σ^0 (5) is shown in Figure 27 where the forward binning scheme appears to lead to an overestimation of scattering areas which in turn reduces CYGNSS NBRCS estimates relative to reference model NBRCS estimates.

The revised DDMA normalization area estimates used as part of CYGNSS's v3.1 data release are derived using the same procedures used in Section IV.B are used while substituting the forward binning scheme with a central binning scheme such that the physical scattering area at delay τ and Doppler f comprises the footprint spanning $\in [\tau - \Delta_\tau/2 \leq \tau < \tau + \Delta_\tau/2, f - \Delta_f/2 \leq f < f + \Delta_f/2]$ thereby limiting maximum delay-Doppler sampling errors to $\Delta_\tau/2$ and delta $\Delta_f/2$ respectively. An example of the physical area solutions using the revised binning scheme is shown in Figure 28.

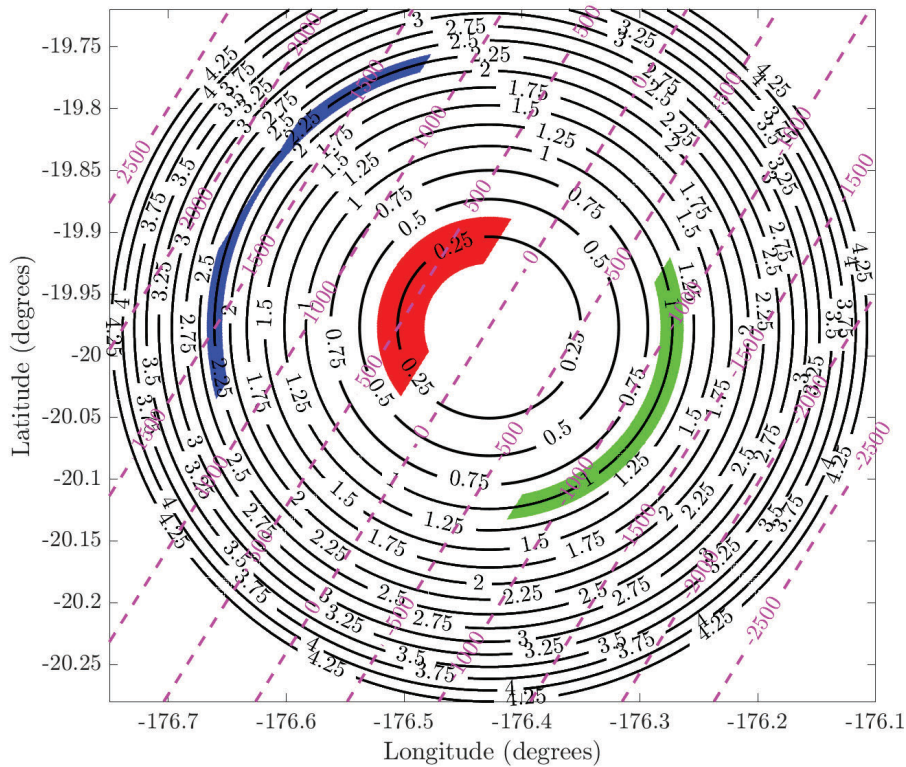


Figure 28. Example of surface grid used to develop physical scattering area DDMs. Iso-delay (Chips) lines are in black, iso-Doppler (Hz) lines are in magenta. For illustrative purposes, the physical area using a **central binning scheme** corresponding to $A(\tau=0.25 \text{ chips}, f=500 \text{ Hz})$ is in red, $A(\tau=1 \text{ chips}, f=1000 \text{ Hz})$ is in green and $A(\tau=2.25 \text{ chips}, f=1500 \text{ Hz})$ is in blue.

It is estimated that the forward binning scheme was associated with a ~22% average overestimation of DDMA normalization areas such that a reduction of A_{tot} significantly improved the correspondence of CYGNSS's NBRCS estimates to reference NBRCS estimates (see Figure 7).

As a result of the switch from forward binning to central binning, the resulting effective area normalization of the DDMA was reduced by 22.36% using a constant scale factor applied to all v.3.1 DDMA effective area look-up-table entries.



REFERENCES

- [1] Gleason, S., Ruf, C.S., OBrien, A.J. and D.S. McKague, "The CYGNSS Level 1 Calibration Algorithm and Error Analysis Based on On-Orbit Measurements," IEEE Journal of Selected Topics in Applied Earth Observations and Remote Sensing, 10.1109/JSTARS.2018.2832981, 2018.
- [2] Zavorotny V. and A. Voronovich (2000), Scattering of GPS Signals from the Ocean with Wind Remote Sensing Application . IEEE Trans. Geosci. Remote Sens., Vol. 38, pp. 951-964, March 2000. DOI: 10.1109/36.841977
- [3] DTU Space, National Space Institute (Denmark). Global Mean Sea Surface.
- [4] Bar-Sever, Y., "A new model for GPS yaw attitude," Journal of Geodesy 70:714-723, 1996.
- [5] Gleason, S., Ruf, C. Clarizia, M.P., OBrien, A. J., "Calibration and Unwrapping of the Normalized Scattering Cross Section for the Cyclone Global Navigation Satellite System", IEEE Trans. Geoscience and Remote Sensing, Vol. 54, No. 5, May 2016.
- [6] Wang, T., Ruf, C., Block, B., McKague, D. and S. Gleason, "Design and Performance of a GPS Constellation Power Monitor System for Improved CYGNSS L1B Calibration," IEEE Journal of Selected Topics in Applied Earth Observations and Remote Sensing, accepted for publication.
- [7] W. A. Marquis, W.A. and D. L. Reigh, "The GPS Block IIR and IIR-M broadcast L-band antenna panel: Its pattern and performance, Navigation, vol. 62, no. 4, pp. 329-347, Dec. 2015.
- [8] Wang, T., Ruf, C., Gleason, S., Block, B., McKague, D. and D. Provost, "Development of GPS constellation power monitor system for high accuracy calibration/validation of the CYGNSS L1B data, 2017 IEEE International Geoscience and Remote Sensing Symposium (IGARSS), Fort Worth, TX, pp. 1008-1011, July 23-28, 2017.
- [9] Wang, T., Ruf, C., Block, B and D. McKague, "Characterization of the transmit power and antenna pattern of the GPS constellation for the CYGNSS mission, 2018 IEEE International Geoscience and Remote Sensing Symposium (IGARSS), Valencia, Spain, July 22-27, 2018.
- [10] Steigenberger, P., Hauschild, A., Thielert, S. and R. Langley, "US Air Force puts more power into GPS Block IIR-M C/A-code, GPS World, vol. 28, no. 4, pp. 8-9, Apr. 2017.
- [11] Thielert, S., Hauschild, A., Steigenberger, P. and R. Langley, "GPS IIR-M L1 transmit power redistribution: Analysis of GNSS receiver and highgain antenna data, Proceedings of the 30th International Technical Meeting of The Satellite Division of the Institute of Navigation, Portland, Oregon, Sept. 2017, pp. 1589-1602.
- [12] Ruf, C.S., Gleason, S. and D.S. McKague, "Assessment of CYGNSS Wind Speed Retrieval Uncertainty," IEEE Journal of Selected Topics in Applied Earth Observations and Remote Sensing, 10.1109/JSTARS.2018.2825948, 2018.
- [13] Jansen, M.A., Ruf, C.S. and S.J. Keihm (1995), TOPEX/Poseidon Microwave Radiometer (TMR): II. Antenna Pattern Correction and Brightness Temperature Algorithm, IEEE Trans. Geosci. Remote Sens., Vol. 33, No. 1, pp. 138-146, January 1995.
- [14] Algorithm Theoretical Basis Document (ATBD): CYGNSS Level 1a DDM Calibration and Error Analysis, April 2018.
- [15] Misra P., and P. Enge, Global Positioning System: Signals, Measurements, and Performance, Ganga Jamuna Press, 2001. ISBN 0-9709544-0-9.
- [16] Ulaby, F. T., Long, D. G., Microwave Radar and Radiometric Remote Sensing, Ann Arbor, MI, USA: Univ. Michigan Press, 2014.
- [17] S. Gleason, M. Al-Khaldi, C. Ruf, D. McKague, T. Wang and A. Russel, "Characterizing and Mitigating Digital Sampling Effects on the CYGNSS Level 1 Calibration," IEEE Transactions on Geoscience and Remote Sensing, (Accepted) October 2021.
- [18] F.T. Ulaby and D.G. Long, Microwave Radar and Radiometric Remote Sensing; University Michigan Press: Ann Arbor, MI, USA, 2014.
- [19] P. Misra and P. Enge, Global Positioning System: Signals, Measurements, and Performance. Ganga Jamuna Press, 2001. ISBN 0-9709544-0-9.
- [20] P. Bechtold, P. Bauer, J.R. Bidlot, C. Cardinali, L. Magnusson, F. Prates and M. Rodwell, "Uncertainty in tropical winds," Meteorology section of ECMWF Newsletter No. 134, Winter



2012/13, pp. 33–37.

- [21] The WAVEWATCH III Development Group (WW3DG), 2016: User manual and system documentation of WAVEWATCH III version 5.16. Tech. Note 329, NOAA/NWS/NCEP/MMAB, College Park, MD, USA, 326 pp.+ Appendices.
- [22] T. Wang, V. U. Zavorotny, J. Johnson, Y. Yi and C. Ruf, "Integration of Cygnss Wind and Wave Observations with the Wavewatch III Numerical Model," IGARSS 2019 - 2019 IEEE International Geoscience and Remote Sensing Symposium, 2019, pp. 8350-8353, doi: 10.1109/IGARSS.2019.8900481.
- [23] T. Wang et al., "Dynamic Calibration of GPS Effective Isotropic Radiated Power for GNSS-Reflectometry Earth Remote Sensing," IEEE Trans. Geosci. Remote. Sens., doi: 10.1109/TGRS.2021.3070238.
- [24] T. Wang et al., "Dynamic Calibration of GPS Effective Isotropic Radiated Power for GNSS-Reflectometry Earth Remote Sensing," IEEE Trans. Geosci. Remote. Sens., doi: 10.1109/TGRS.2021.3070238.



Appendix – Level 1 Data Dictionary

netCDF Name	netCDF Long Name	netCDF Type	Units	netCDF Dimensions	Comment
Global Values					
time_coverage_start	<none>	file attribute, string	<none>	<none>	ddm_timestamp_utc of the first sample in the file in ISO-8601 form
time_coverage_end	<none>	file attribute, string	<none>	<none>	ddm_timestamp_utc of the last sample in the file in ISO-8601 form
time_coverage_duration	<none>	file attribute, string	<none>	<none>	The time interval between time_coverage_start and time_coverage_end in ISO1806 form
time_coverage_resolution	<none>	file attribute, string	<none>	<none>	The nominal time interval between samples in ISO1806 form
spacecraft_id	CCSDS spacecraft identifier	short	1	<none>	The CCSDS spacecraft identifier: 0xF7 (247): CYGNSS 1 0xF9 (249): CYGNSS 2 0x2B (43): CYGNSS 3 0x2C (44): CYGNSS 4 0x2F (47): CYGNSS 5 0x36 (54): CYGNSS 6 0x37 (55): CYGNSS 7 0x49 (73): CYGNSS 8 0x00 (0): E2ES 0x0E (14): engineering model 0x0D (15): default 0xFF (255): unknown
spacecraft_num	CYGNSS spacecraft number	byte	1	<none>	The CYGNSS spacecraft number: Ranges from 1 through 8 and 99. 1 through 8 are on-orbit spacecraft. 99 is the CYGNSS end-to-end simulator.
ddm_source	Level 0 data source	byte	<none>	<none>	The source of the Level 0 DDM raw counts and metadata. 0 = End-End Simulator (E2ES) 1 = GPS signal simulator 2 = CYGNSS spacecraft 3 = Source unknown



ddm_time_type_selector	DDM sample time type selector	byte	<none>	<none>	Determines the position of ddm_timestamp_utc relative to the DDM sampling period. Set to "Middle of DDM sampling period" for nominal science operations. Other settings are used for pre-launch testing only. 0 = Start of DDM sampling period (used for pre-launch testing only) 1 = Middle of DDM sampling period 2 = End of DDM sampling period (used for pre-launch testing only) 3 = pvt_timestamp_utc (used for pre-launch testing only)
delay_resolution	DDM delay bin resolution	float	1	<none>	DDM delay bin resolution in chips. One chip is equal to 1/1,023,000 seconds.
dopp_resolution	DDM Doppler bin resolution	float	s-1	<none>	DDM Doppler bin resolution in Hz
l1_algorithm_version	<none>	file attribute, string	<none>	<none>	The version number of the L1 processing algorithm.
l1_data_version	<none>	file attribute, string	<none>	<none>	The version number of the L1 data.
lna_data_version	<none>	file attribute, string	<none>	<none>	The version number of the LNA data lookup table.
eff_scatter_version	<none>	file attribute, string	<none>	<none>	The version number of the effective scattering area lookup table.
nadir_ant_data_version	<none>	file attribute, string	<none>	<none>	The version number of the nadir antenna data lookup table.
zenith_ant_data_version	<none>	file attribute, string	<none>	<none>	The version number of the zenith antenna data lookup table.
ant_temp_version	<none>	file attribute, string	<none>	<none>	The version number of the radiometric antenna temperature lookup table.
prn_sv_maps_version	<none>	file attribute, string	<none>	<none>	The version number of the PRN to SV lookup table.
gps_eirp_parameter_version	<none>	file attribute, string	<none>	<none>	The version number of the GPS effective isotropic radiated power parameter lookup table



land_mask_version	<none>	file attribute, string	<none>	<none>	The version number of the Earth land mask lookup table.
near_land_mask_version	<none>	file attribute, string	<none>	<none>	The version number of the Earth near-land mask lookup table.
very_near_land_mask_version	<none>	file attribute, string	<none>	<none>	The version number of the Earth very-near-land mask lookup table.
open_ocean_mask_version	<none>	file attribute, string	<none>	<none>	The version number of the open ocean mask lookup table.
ddm_a2d_version	<none>	file attribute, string	<none>	<none>	The version number of the DDM digital to analog power conversion lookup table.
milky_way_version	<none>	file attribute, string	<none>	<none>	The version number of the Milky Way mask lookup table.
fresnel_coeff_version	<none>	file attribute, string	<none>	<none>	The version number of the Fresnel coefficient lookup table.
brcs_uncert_lookup_version	<none>	file attribute, string	<none>	<none>	The version number of the BRCS uncertainty lookup table.
ddma_les_sel_lookup_version	<none>	file attribute, string	<none>	<none>	The version number of the NBRCS (formerly known as DDMA) and LES bin selection table.
mean_sea_surface_version	<none>	file attribute, string	<none>	<none>	The version of the mean sea surface lookup table.
zenith_specular_ratio_gain_version	<none>	file attribute, string	<none>	<none>	The version of the zenith specular ratio gain lookup table.
zenith_calibration_params_version	<none>	file attribute, string	<none>	<none>	The version of the zenith calibration parameters lookup table.
anomalous_sampling_periods_version	<none>	file attribute, string	<none>	<none>	The version of the anomalous sampling periods lookup table.
noise_floor_correction_version	<none>	file attribute, string	<none>	<none>	The version of the noise floor correction factor lookup table.
zenith_sig_i2_q2_correction_version	<none>	file attribute, string	<none>	<none>	The version of the zenith signal I2 Q2 correction factor lookup table.
ddm_nbrcs_scale_factor_version	<none>	file attribute, string	<none>	<none>	The version of the DDM NBRCS correction factor lookup table.



eirp_scale_factor_version	<none>	file attribute, string	<none>	<none>	The version of the EIRP correction factor for the Feb 14, 2020 power shift lookup table.
bin_ratio_qc_version	<none>	file attribute, string	<none>	<none>	The version of the bin ratio QC correction factor lookup table.
per_bin_ant_version	<none>	file attribute, string	<none>	<none>	The version of the per-bin antenna gain lookup table.
Per-Sample Values					
ddm_timestamp_utc	DDM sample timestamp - UTC	double	seconds since time_coverage_start	sample	DDM sample time. The number of seconds since time_coverage_start with nanosecond resolution. Its position relative to the DDM sampling period is determined by ddm_time_type_selector. Some metadata required for DDM calibration are generated relative to pvt_timestamp_utc or att_timestamp_utc. These metadata are interpolated to ddm_timestamp_utc before being used for DDM calibration. Note that the DDM sampling period is not synchronized with the UTC change of second and can occur at any time relative to the UTC change of second.
ddm_timestamp_gps_week	DDM sample timestamp - GPS week	int	week	sample	The GPS week number of ddm_timestamp_utc
ddm_timestamp_gps_sec	DDM sample timestamp - GPS seconds	double	second	sample	The GPS second of week of ddm_timestamp_utc with nanosecond resolution
pvt_timestamp_utc	PVT timestamp - UTC	double	seconds since time_coverage_start	sample	The spacecraft position and velocity epoch. The number of seconds since time_coverage_start with nanosecond resolution. This is the timestamp of the position and velocity reported by the DDMI. This is also the timestamp of the most recent GPS pulse per second.



pvt_timestamp_gps_week	PVT timestamp - GPS Week	int	week	sample	The GPS week number of pvt_timestamp_utc
pvt_timestamp_gps_sec	PVT timestamp - GPS Seconds	double	second	sample	The GPS second of week of pvt_timestamp_utc with nanosecond resolution.
att_timestamp_utc	Attitude timestamp - UTC	double	seconds since time_coverage_start	sample	The spacecraft attitude epoch. The number of seconds since time_coverage_start with nanosecond resolution. This is the timestamp of the spacecraft attitude reported by the spacecraft attitude determination system.
att_timestamp_gps_week	Attitude timestamp - GPS Week	int	week	sample	The GPS week number of att_timestamp_utc
att_timestamp_gps_sec	Attitude timestamp - GPS Seconds	double	second	sample	The GPS second of week of att_timestamp_utc with nanosecond resolution
sc_pos_x	Spacecraft position X at DDM sample time	int	meter	sample	The X component of the spacecraft WGS84 reference frame ECEF position, in meters, at ddm_timestamp_utc. Fill value is -99999999.
sc_pos_y	Spacecraft position Y at DDM sample time	int	meter	sample	The Y component of the spacecraft WGS84 reference frame ECEF position, in meters, at ddm_timestamp_utc. Fill value is -99999999.
sc_pos_z	Spacecraft position Z at DDM sample time	int	meter	sample	The Z component of the spacecraft WGS84 reference frame ECEF position, in meters, at ddm_timestamp_utc. Fill value is -99999999.
sc_vel_x	Spacecraft velocity X at DDM sample time	int	meter s-1	sample	The X component of the spacecraft WGS84 reference frame ECEF velocity, in m/s, at ddm_timestamp_utc
sc_vel_y	Spacecraft velocity Y at DDM sample time	int	meter s-1	sample	The Y component of the spacecraft WGS84 reference frame ECEF velocity, in m/s, at ddm_timestamp_utc
sc_vel_z	Spacecraft velocity Z at DDM sample time	int	meter s-1	sample	The Z component of the spacecraft WGS84 reference frame ECEF velocity, in m/s, at ddm_timestamp_utc.



ATBD Level 1B DDM Calibration

sc_pos_x_pvt	Spacecraft position X at PVT time	int	meter	sample	The X component of the spacecraft WGS84 reference frame ECEF position, in meters, at pvt_timestamp_utc. Fill value is -99999999.
sc_pos_y_pvt	Spacecraft position Y at PVT time	int	meter	sample	The Y component of the spacecraft WGS84 reference frame ECEF position, in meters, at pvt_timestamp_utc. Fill value is -99999999.
sc_pos_z_pvt	Spacecraft position Z at PVT time	int	meter	sample	The Z component of the spacecraft WGS84 reference frame ECEF position, in meters, at pvt_timestamp_utc. Fill value is -99999999.
sc_vel_x_pvt	Spacecraft velocity X at PVT time	int	meter s-1	sample	The X component of the spacecraft WGS84 reference frame ECEF velocity, in m/s, at pvt_timestamp_utc
sc_vel_y_pvt	Spacecraft velocity Y at PVT time	int	meter s-1	sample	The Y component of the spacecraft WGS84 reference frame ECEF velocity, in m/s, at pvt_timestamp_utc
sc_vel_z_pvt	Spacecraft velocity Z at PVT time	int	meter s-1	sample	The Z component of the spacecraft WGS84 reference frame ECEF velocity, in m/s, at pvt_timestamp_utc



nst_att_status	NST attitude status	byte	<none>	sample	The nano star tracker attitude status. 0 = OK 1 = NOT_USED2 2 = BAD 3 = TOO_FEW_STARS 4 = QUEST_FAILED 5 = RESIDUALS_TOO_HIGH 6 = TOO_CLOSE_TO_EDGE 7 = PIX_AMP_TOO_LOW 8 = PIX_AMP_TOO_HIGH 9 = BACKGND_TOO_HIGH 10 = TRACK_FAILURE 11 = PIX_SUM_TOO_LOW 12 = UNUSED 13 = TOO_DIM_FOR_STARID 14 = TOO_MANY_GROUPS 15 = TOO_FEW_GROUPS 16 = CHANNEL_DISABLED 17 = TRACK_BLK_OVERLAP 18 = OK_FOR_STARID 19 = TOO_CLOSE_TO_OTHER 20 = TOO_MANY_PIXELS 21 = TOO_MANY_COLUMNS 22 = TOO_MANY_ROWS
sc_roll	Spacecraft attitude roll angle at DDM sample time	float	radian	sample	Spacecraft roll angle relative to the orbit frame, in radians at ddm_timestamp_utc
sc_pitch	Spacecraft attitude pitch angle at DDM sample time	float	radian	sample	Spacecraft pitch angle relative to the orbit frame, in radians at ddm_timestamp_utc
sc_yaw	Spacecraft attitude yaw angle at DDM sample time	float	radian	sample	Spacecraft yaw angle relative to the orbit frame, in radians at ddm_timestamp_utc
sc_roll_att	Spacecraft attitude roll angle at attitude time	float	radian	sample	Spacecraft roll angle relative to the orbit frame, in radians at att_timestamp_utc
sc_pitch_att	Spacecraft attitude pitch angle at attitude time	float	radian	sample	Spacecraft pitch angle relative to the orbit frame, in radians at att_timestamp_utc



ATBD Level 1B DDM Calibration

sc_yaw_att	Spacecraft attitude yaw angle at attitude time	float	radian	sample	Spacecraft yaw angle relative to the orbit frame, in radians at att_timestamp_utc
sc_lat	Sub-satellite point latitude	float	degrees_north	sample	Subsatellite point latitude, in degrees North, at ddm_timestamp_utc
sc_lon	Sub-satellite point longitude	float	degrees_east	sample	Subsatellite point longitude, in degrees East, at ddm_timestamp_utc
sc_alt	Spacecraft altitude	int	meter	sample	Spacecraft altitude above WGS-84 ellipsoid, in meters, at ddm_timestamp_utc
commanded_sc_roll	Commanded spacecraft attitude roll angle	float	radians	sample	Commanded spacecraft attitude roll angle, in radians at ddm_timestamp_utc. This value is updated every 10 seconds from the ENG_HI packet.
rx_clk_bias	GPS receiver clock bias	float	meter	sample	The receiver clock bias (in seconds) multiplied by the speed of light as reported by the DDMI, interpolated to ddm_timestamp_utc, in meters.
rx_clk_bias_rate	GPS receiver clock bias rate	float	meter s ⁻¹	sample	The receiver clock bias rate (in seconds/second) multiplied by the speed of light as reported by the DDMI, interpolated to ddm_timestamp_utc, in m/s.
rx_clk_bias_pvt	GPS receiver clock bias at PVT time	float	meter	sample	The receiver clock bias (in seconds) multiplied by the speed of light as reported by the DDMI at pvt_timestamp_utc, in meters.
rx_clk_bias_rate_pvt	GPS receiver clock bias rate at PVT time	float	meter s ⁻¹	sample	The receiver clock bias rate (in seconds/second) multiplied by the speed of light as reported by the DDMI, at pvt_timestamp_utc, in m/s.
lna_temp_nadir_starboard	Starboard antenna LNA temperature	float	degree_Celsius	sample	The temperature of the starboard antenna LNA at ddm_timestamp_utc, in degrees C.
lna_temp_nadir_port	Port antenna LNA temperature	float	degree_Celsius	sample	The temperature of the port antenna LNA at ddm_timestamp_utc, in degrees C.
lna_temp_zenith	Zenith antenna LNA temperature	float	degree_Celsius	sample	The temperature of the zenith antenna LNA at ddm_timestamp_utc, in degrees C.



ATBD Level 1B DDM Calibration

ddm_end_time_offset	DDM end time offset	int	1e-9 s	sample	For diagnostic use only. See UM document 148-0372 CYGNSS L1 netCDF Diagnostic Variables for more information.
bit_ratio_lo_hi_starboard	Starboard low/high bit counter ratio	float	1	sample	Bin ratio of the of the starboard antenna defined as $(plus_1_cnts + minus_1_cnts) / (plus_3_cnts + minus_3_cnts)$.
bit_ratio_lo_hi_port	Port low/high bit counter ratio	float	1	sample	Bin ratio of the of the port antenna defined as $(plus_1_cnts + minus_1_cnts) / (plus_3_cnts + minus_3_cnts)$.
bit_ratio_lo_hi_zenith	Zenith low/high bit counter ratio	float	1	sample	Bin ratio of the of the zenith antenna defined as $(plus_1_cnts + minus_1_cnts) / (plus_3_cnts + minus_3_cnts)$.
bit_null_offset_starboard	Starboard bit count null offset	float	1	sample	For diagnostic use only. See UM document 148-0372 CYGNSS L1 netCDF Diagnostic Variables for more information.
bit_null_offset_port	Port bit count null offset	float	1	sample	For diagnostic use only. See UM document 148-0372 CYGNSS L1 netCDF Diagnostic Variables for more information.
bit_null_offset_zenith	Zenith bit count null offset	float	1	sample	For diagnostic use only. See UM document 148-0372 CYGNSS L1 netCDF Diagnostic Variables for more information.
status_flags_on_e_hz	1 Hz status flags	int	<none>	sample	One Hz status flags. These flags apply to all four DDMs. 1 indicates presence of condition. Flag masks: 1 = Milky way in zenith antenna field of view 2 = Sun in zenith antenna field of view 4 = Sub-satellite point over open ocean 8 = Subsatellite point latitude ascending, i.e. sc_lat is increasing.
Per-DDM Values					
prn_code	GPS PRN code	byte	1	sample, ddm	The PRN code of the GPS signal associated with the DDM. Ranges from 0 to 32. 0 = reflectometry channel idle. 1 through 32 = GPS PRN codes.
sv_num	GPS space	int	1	sample,	The GPS unique space vehicle



ATBD Level 1B DDM Calibration

	vehicle number			ddm	number that transmitted prn_code.
track_id	DDM track ID	int	1	sample, ddm	A track is a temporally contiguous series of DDMs that have the same prn_code. Each track in the file is assigned a unique track_id starting with one. track_id ranges from 1 to N, where N is the total number of tracks in the file.
ddm_ant	DDM antenna	byte	<none>	sample, ddm	The antenna that received the reflected GPS signal associated with the DDM. 0 = none 1 = zenith (never used) 2 = nadir_starboard 3 = nadir_port
zenith_code_phase	Zenith signal code phase	float	1	sample, ddm	The DDMI-measured code phase of the direct GPS signal for prn_code interpolated to ddm_timestamp_utc. $0 \leq \text{zenith_code_phase} < 1023.0$.
sp_ddmi_delay_correction	Correction to DDMI specular point delay	float	1	sample, ddm	For diagnostic use only. See UM document 148-0372 CYGNSS L1 netCDF Diagnostic Variables for more information.
sp_ddmi_dopp_correction	Correction to DDMI specular point Doppler	float	s-1	sample, ddm	For diagnostic use only. See UM document 148-0372 CYGNSS L1 netCDF Diagnostic Variables for more information.
add_range_to_sp	Additional range to specular point at DDM sample time	float	1	sample, ddm	For diagnostic use only. See UM document 148-0372 CYGNSS L1 netCDF Diagnostic Variables for more information.
add_range_to_sp_pvt	Additional range to specular point at PVT time	float	1	sample, ddm	For diagnostic use only. See UM document 148-0372 CYGNSS L1 netCDF Diagnostic Variables for more information.
sp_ddmi_dopp	DDMI Doppler at specular point	float	s-1	sample, ddm	For diagnostic use only. See UM document 148-0372 CYGNSS L1 netCDF Diagnostic Variables for more information.
sp_fsw_delay	Flight software specular	float	1	sample, ddm	For diagnostic use only. See UM document 148-0372 CYGNSS L1 netCDF Diagnostic Variables for



ATBD Level 1B DDM Calibration

	point delay				more information.
sp_delay_error	Flight software specular point delay error	float	1	sample, ddm	For diagnostic use only. See UM document 148-0372 CYGNSS L1 netCDF Diagnostic Variables for more information.
sp_dopp_error	Flight software specular point Doppler error	float	s-1	sample, ddm	For diagnostic use only. See UM document 148-0372 CYGNSS L1 netCDF Diagnostic Variables for more information.
fsw_comp_delay_shift	Flight software DDM compression delay shift	float	1	sample, ddm	For diagnostic use only. See UM document 148-0372 CYGNSS L1 netCDF Diagnostic Variables for more information.
fsw_comp_dopp_shift	Flight software DDM compression Doppler shift	float	s-1	sample, ddm	For diagnostic use only. See UM document 148-0372 CYGNSS L1 netCDF Diagnostic Variables for more information.
prn_fig_of_merit	PRN selection Figure of Merit	byte	1	sample, ddm	The RCG Figure of Merit (FOM) for the DDM. Ranges from 0 through 15. The DDMI selects the four strongest specular points (SP) for DDM production. It ranks the strength of SPs using an antenna RCG map. The map converts the position of the SP in antenna azimuth and declination angles to an RCG FOM. 0 represents the least FOM value. 15 represents the greatest FOM value.
tx_clk_bias	GPS transmitter clock bias	float	meter	sample, ddm	The GPS spacecraft (sv_num) clock time minus GPS constellation time in seconds times the speed of light, in meters.
sp_lat	Specular point latitude	float	degrees_north	sample, ddm	Specular point latitude, in degrees North, at ddm_timestamp_utc
sp_lon	Specular point longitude	float	degrees_east	sample, ddm	Specular point longitude, in degrees East, at ddm_timestamp_utc



ATBD Level 1B DDM Calibration

sp_alt	Specular point altitude	float	meter	sample, ddm	Altitude of the specular point relative to the WGS 84 datum in meters, at ddm_timestamp_utc, as calculated on the ground. Note that an approximated DTU10 mean sea surface height model is used to calculate the specular point altitude.
sp_pos_x	Specular point position X	int	meter	sample, ddm	The X component of the specular point position in the ECEF coordinate system, in meters, at ddm_timestamp_utc, as calculated on the ground. Fill value is -99999999.
sp_pos_y	Specular point position Y	int	meter	sample, ddm	The Y component of the specular point position in the ECEF coordinate system, in meters, at ddm_timestamp_utc, as calculated on the ground. Fill value is -99999999.
sp_pos_z	Specular point position Z	int	meter	sample, ddm	The Z component of the specular point position in the ECEF coordinate system, in meters, at ddm_timestamp_utc, as calculated on the ground. Fill value is -99999999.
sp_vel_x	Specular point velocity X	int	meter s-1	sample, ddm	The X component of the specular point velocity in the ECEF coordinate system, in m/s, at ddm_timestamp_utc, as calculated on the ground.
sp_vel_y	Specular point velocity Y	int	meter s-1	sample, ddm	The Y component of the specular point velocity in the ECEF coordinate system, in m/s, at ddm_timestamp_utc, as calculated on the ground.
sp_vel_z	Specular point velocity Z	int	meter s-1	sample, ddm	The Z component of the specular point velocity in the ECEF coordinate system, in m/s, at ddm_timestamp_utc, as calculated on the ground.
sp_inc_angle	Specular point incidence angle	float	degree	sample, ddm	The specular point incidence angle, in degrees, at ddm_timestamp_utc. This is the angle between the line normal to the Earth's surface at the specular point and the line extending from the specular point to the spacecraft. See UM Doc. 148-0336, CYGNSS Science Data



					Processing Coordinate Systems Definitions.
sp_theta_orbit	Specular point orbit frame theta angle	float	degree	sample, ddm	The angle between the orbit frame +Z axis and the line extending from the spacecraft to the specular point, in degrees, at ddm_timestamp_utc. See UM Doc. 148-0336, CYGNSS Science Data Processing Coordinate Systems Definitions.
sp_az_orbit	Specular point orbit frame azimuth angle	float	degree	sample, ddm	Let line A be the line that extends from the spacecraft to the specular point at ddm_timestamp_utc. Let line B be the projection of line A onto the orbit frame XY plane. sp_az_orbit is the angle between the orbit frame +X axis (the velocity vector) and line B, in degrees, at ddm_timestamp_utc. See UM Doc. 148-0336, CYGNSS Science Data Processing Coordinate Systems Definitions.
sp_theta_body	Specular point body frame theta angle	float	degree	sample, ddm	The angle between the spacecraft body frame +Z axis and the line extending from the spacecraft to the specular point, in degrees, at ddm_timestamp_utc. See UM Doc. 148-0336, CYGNSS Science Data Processing Coordinate Systems Definitions.
sp_az_body	Specular point body frame azimuth angle	float	degree	sample, ddm	Let line A be the line that extends from the spacecraft to the specular point, at ddm_timestamp_utc. Let line B be the projection of line A onto the spacecraft body frame XY plane. sp_az_body is the angle between the spacecraft body frame +X axis and line B, in degrees, at ddm_timestamp_utc. See UM Doc. 148-0336, CYGNSS Science Data Processing Coordinate Systems Definitions.



ATBD Level 1B DDM Calibration

sp_rx_gain	Specular point Rx antenna gain	float	dBi	sample, ddm	The receive antenna gain in the direction of the specular point, in dBi, at ddm_timestamp_utc.
gps_eirp	GPS effective isotropic radiated power	float	watt	sample, ddm	The effective isotropic radiated power (EIRP) of the L1 C/A code signal within ± 1 MHz of the L1 carrier radiated by space vehicle, sv_num, in the direction of the specular point, in Watts, at ddm_timestamp_utc. Variations in GPS transmit power are tracked by the direct signal power measured by the navigation receiver. One second samples are smoothed by a +/- 10 second running average.
static_gps_eirp	Static GPS effective isotropic radiated power	float	watt	sample, ddm	Heritage version of gps_eirp (v2.1 and earlier) that assumed a static value for the power level of the L1 signal transmitted by the GPS satellite, prior to implementation of dynamic gps_eirp monitoring in August 2018.
gps_tx_power_db_w	GPS SV transmit power	float	dbW	sample, ddm	Power input to SV Tx antenna. Referenced from the heritage version of gps_eirp (v2.1 and earlier).
gps_ant_gain_db_i	GPS SV transmit antenna gain	float	dBi	sample, ddm	SV antenna gain in the direction of the specular point. Referenced from the heritage version of gps_eirp (v2.1 and earlier).
gps_off_boresight_angle_deg	GPS off boresight angle	float	degree	sample, ddm	SV antenna off boresight angle in the direction of the specular point
ddm_snr	DDM signal to noise ratio	float	dB	sample, ddm	$10\log(S_{max}/N_{avg})$, where S_{max} is the maximum value (in raw counts) in a single DDM bin and N_{avg} is the the average per-bin raw noise counts. ddm_snr is in dB, at ddm_timestamp_utc.
ddm_noise_floor	DDM noise floor	float	1	sample, ddm	For non-black-body DDMs: Is equal to the average bin raw counts in the first 45 delay rows of the uncompressed 20 x 128 DDM, in counts, at ddm_timestamp_utc. For black body DDMs: Is equal to the average bin raw counts in all 128



ATBD Level 1B DDM Calibration

					delay rows of the uncompressed 20 x 128 DDM, in counts, at ddm_timestamp_utc.
ddm_noise_floor_corrected	DDM noise floor corrected	float	1	sample, ddm	The ddm_noise_floor after a correction factor, based on the nadir antenna bin ratio, has been applied.
noise_correction	DDM noise floor correction factor	float	1	sample, ddm	The correction factor applied with ddm_noise_floor = (ddm_noise_floor_uncorrected * noise_correction).
inst_gain	Instrument gain	float	1	sample, ddm	The black body noise counts divided by the sum of the black body power and the instrument noise power, in count/W, at ddm_timestamp_utc.
lna_noise_figure	LNA noise figure	float	dB	sample, ddm	The LNA noise figure, in dB, at ddm_timestamp_utc. Estimated from pre-launch characterization of LNA performance as a function of LNA temperature.
rx_to_sp_range	Rx to specular point range	int	meter	sample, ddm	The distance between the CYGNSS spacecraft and the specular point, in meters, at ddm_timestamp_utc.
tx_to_sp_range	Tx to specular point range	int	meter	sample, ddm	The distance between the GPS spacecraft and the specular point, in meters, at ddm_timestamp_utc.
tx_pos_x	GPS Tx position X	int	meter	sample, ddm	The X component of the GPS spacecraft WGS84 reference frame ECEF position, in meters, at ddm_timestamp_utc. Fill value is -99999999.
tx_pos_y	GPS Tx position Y	int	meter	sample, ddm	The Y component of the GPS spacecraft WGS84 reference frame ECEF position, in meters, at ddm_timestamp_utc. Fill value is -99999999.
tx_pos_z	GPS Tx position Z	int	meter	sample, ddm	The Z component of the GPS spacecraft WGS84 reference frame ECEF position, in meters, at ddm_timestamp_utc. Fill value is -99999999.
tx_vel_x	GPS Tx velocity X	int	meter s ⁻¹	sample, ddm	The X component of the GPS spacecraft WGS84 reference frame ECEF velocity in meters, at ddm_timestamp_utc



ATBD Level 1B DDM Calibration

tx_vel_y	GPS Tx velocity Y	int	meter s-1	sample, ddm	The Y component of the GPS spacecraft WGS84 reference frame ECEF velocity in meters, at ddm_timestamp_utc
tx_vel_z	GPS Tx velocity Z	int	meter s-1	sample, ddm	The Z component of the GPS spacecraft WGS84 reference frame ECEF velocity in meters, at ddm_timestamp_utc
bb_nearest	Time to most recent black body reading	float	second	sample, ddm	The time between ddm_timestamp_utc and the ddm_timestamp_utc of the closest (in time) black body reading, in signed seconds. A positive value indicates that the black body reading occurred after ddm_timestamp_utc. A negative value indicates that the block body reading occurred before ddm_timestamp_utc.
fresnel_coeff	Fresnel power reflection coefficient at specular point	float	1	sample, ddm	The SQUARE of the left hand circularly polarized Fresnel electromagnetic voltage reflection coefficient at 1575 MHz for a smooth ocean surface at the specular point location and incidence angle. See UM document 148-0361 Fresnel Coefficient Calculation for more information.
ddm_nbrcs	Normalized BRCS	float	1	sample, ddm	Normalized BRCS of a 3 delay x 5 Doppler bin box that include the specular point bin. The specular point bin is in the top (least delay) row and the center Doppler column of the 3 x 5 box.
ddm_les	Leading edge slope	float	1	sample, ddm	Leading edge slope of a 3 delay x 5 Doppler bin box that include the specular point bin. The specular point bin is in the top (least delay) row and the center Doppler column of the 3 x 5 box.
nbrcs_scatter_area	NBRCS scattering area	float	meter ²	sample, ddm	The scattering area of the 3 x 5 region of the ddm used to calculate ddm_nbrcs.
les_scatter_area	LES scattering area	float	meter ²	sample, ddm	The scattering area of the 3 x 5 region of the ddm used to calculate ddm_les.
brcs_ddm_peak_bin_delay_row	BRCS DDM peak bin delay	byte	1	sample, ddm	The zero-based delay row of the peak value in the bistatic radar cross section DDM (brcs).



ATBD Level 1B DDM Calibration

	row				Ranges from 0 to 16.
brcs_ddm_peak_bin_dopp_col	BRCS DDM peak bin Doppler column	byte	1	sample, ddm	The zero-based Doppler column of the peak value in the bistatic radar cross section DDM (brcs). Ranges from 0 to 10.
brcs_ddm_sp_bin_delay_row	BRCS DDM specular point delay row	float	1	sample, ddm	The zero-based delay row of the specular point delay in the bistatic radar cross section DDM (brcs). Note that this is a floating point value.
brcs_ddm_sp_bin_dopp_col	BRCS DDM specular point Doppler column	float	1	sample, ddm	The zero-based Doppler column of the specular point Doppler in the bistatic radar cross section DDM (brcs). Note that this is a floating point value.
ddm_brcs_uncertainty	DDM BRCS uncertainty	float	1	sample, ddm	Uncertainty of the BRCS.
bb_power_temperature_density	Black Body Power Temperature Density	float	Counts/Kelvin	sample, ddm	Raw counts of detected power radiated by the blackbody calibration target, divided by receiver gain and blackbody physical temperature in Kelvins, gives the detected power per unit absolute temperature.
zenith_sig_i2q2	Zenith Signal I2Q2	int	1	sample, ddm	Raw counts of detected power in direct GPS L1 C/A signal received by zenith navigation antenna and detected by navigation receiver.
zenith_sig_i2q2_corrected	Zenith Signal I2Q2 Corrected	float	1	sample, ddm	The zenith_sig_i2q2 after a correction factor, based on the zenith antenna bin ratio, has been applied.
zenith_sig_i2q2_mult_correction	Zenith Signal I2Q2 Multiplicative Correction Factor	float	1	sample, ddm	The multiplicative correction factor applied with $zenith_sig_i2q2_corrected = 10 * \log_{10}(zenith_sig_i2q2 * zenith_sig_i2q2_mult_correction) - zenith_sig_i2q2$ add correction.
zenith_sig_i2q2_add_correction	Zenith Signal I2Q2 Additive Correction Factor	float	1	sample, ddm	The additive correction factor applied with $zenith_sig_i2q2_corrected = 10 * \log_{10}(zenith_sig_i2q2 * zenith_sig_i2q2_mult_correction) - zenith_sig_i2q2$ add correction.
starboard_gain	The Nadir-	int	dB	sample, ddm	The Nadir-Starboard Gain Setting



ATBD Level 1B DDM Calibration

_setting	Starboard Gain Setting				(dB, 0=Automatic)
port_gain_setting	The Nadir-Port Gain Setting	int	dB	sample,ddm	The Nadir-Port Gain Setting (dB, 0=Automatic)
ddm_kurtosis	DDM Kurtosis	float	1	sample,ddm	The kurtosis of the DDM noise floor. For diagnostic use only. See UM document 148-0347 DDM RFI Algorithm for more information.
quality_flags	Per-DDM quality flags 1	int	<none>	sample, ddm	First group of the Per-DDM quality flags. 1 indicates presence of condition. More quality flags can be found in quality_flags_2. Flag bit masks:
					1/0x00000001 (Bit 01) = poor_overall_quality: The logical OR of the following flags. If any one of the following flags are set then poor_overall_quality will be set: large_sc_attitude_err, black_body_ddm, ddmi_reconfigured, spacewire_crc_invalid, ddm_is_test_pattern, channel_idle, low_confidence_ddm_noise_floor, sp_over_land, sp_very_near_land, large_step_noise_floor, large_step_lna_temp, direct_signal_in_ddm, low_confidence_gps_eirp_estimate, rfi_detected, brcs_ddm_sp_bin_delay_error, brcs_sp_bin_dopp_error, gps_pvt_sp3_error, sp_non_existent_error, brcs_lut_range_error, ant_data_lut_range_error, bb_framing_error, fsw_comp_shift_error, sc_altitude_out_of_nominal_range, anomalous_sampling_period, invalid_roll_state, incorrect_ddmi_antenna_selection(quality_flags_2), sp_in_sidelobe(quality_flags_2), fatal_nst_outage(quality_flags_2),



					<p>low_zenith_ant_gain(quality_flags_2), poor_bb_quality(quality_flags_2) , poor_quality_bin_ratio(quality_flags_2) :</p>
					<p>2/0x00000002 (Bit 02) = s_band_powered_up: Set if S-band transmitter is powered up.</p>
					<p>4/0x00000004 (Bit 03) = small_sc_attitude_err: Set if the absolute value of the spacecraft roll is between 1 and 30 degrees, the pitch is between 1 and 10 degrees, or the yaw is between 1 and 5 degrees.</p>
					<p>8/0x00000008 (Bit 04) = large_sc_attitude_err: Set if the absolute value of the spacecraft roll is greater than or equal to 30 degrees, the pitch is greater than or equal to 10 degrees, or the yaw is greater than or equal to 5 degrees.</p>
					<p>16/0x00000010 (Bit 05) = black_body_ddm: Set if the black body load was selected during the DDM sampling period.</p>
					<p>32/0x00000020 (Bit 06) = ddmi_reconfigured: Set if the DDMI was reconfigured during the DDM sampling period.</p>
					<p>64/0x00000040 (Bit 07) = spacewire_crc_invalid: Set if the DDM CRC transmitted from the DDMI to the spacecraft computer was not valid.</p>
					<p>128/0x00000080 (Bit 08) = ddm_is_test_pattern: Set if the</p>



					DDM is a test pattern generated by the DDMI.
					256/0x00000100 (Bit 09) = channel_idle: Set if this reflectometry channel was not tracking a PRN.
					512/0x00000200 (Bit 10) = low_confidence_ddm_noise_floor: Set if the difference between this DDM noise floor and the previous DDM noise floor is greater than 10%.
					1024/0x00000400 (Bit 11) = sp_over_land: Set if the specular point is over land. Referenced using a map with 0.1 degree lat/lon bins. Coastline features or islands smaller than bin size may not be properly captured.
					2048/0x00000800 (Bit 12) = sp_very_near_land: Set if the specular point is within 25 km of land. Referenced using a map with 0.1 degree lat/lon bins.
					4096/0x00001000 (Bit 13) = sp_near_land: Set if the specular point is within 50 km of land. Referenced using a map with 0.1 degree lat/lon bins.
					8192/0x0002000 (Bit 14) = large_step_noise_floor: Set if the difference between this DDM noise floor and the previous DDM noise floor is greater than 0.24 dB.
					16384/0x00004000 (Bit 15) = large_step_lna_temp: Set if the LNA temperature rate of change is greater than 1 degree C per minute.
					32768/0x00008000 (Bit 16) = direct_signal_in_ddm: Set if the absolute value of the difference between direct signal code phase and the DDM signal code phase is less than or equal to four.
					65536/0x00010000 (Bit 17) = low_confidence_gps_eirp_estimate: Set when there is low



					confidence in the GPS effective isotropic radiated power estimate.
					131072/0x00020000 (Bit 18) = rfi_detected: Set when the kurtosis of the DDM noise floor deviates from pure Gaussian (3.0) by more than 1.0.
					262144/0x00040000 (Bit 19) = brcs_ddm_sp_bin_delay_error. Set if the calculated specular point bin zero-based delay row is less than 6 or greater than 10.
					524288/0x00080000 (Bit 20) = brcs_ddm_sp_bin_dopp_error. Set if the calculated specular point bin zero-based Doppler column is less than 4 or greater than 6.
					1048576/0x00100000 (Bit 21) = neg_brcs_value_used_for_nbrcs. Set if any bin in the 3 x 5 brcs area used to calculate ddm_nbrcs has a negative value.
					2097152/0x00200000 (Bit 22) = gps_pvt_sp3_error. Cannot calculate GPS SV position/velocity/time from SP3 file.
					4194304/0x00400000 (Bit 23) = sp_non_existent_error. Specular point does not exist.
					8388608/0x00800000 (Bit 24) = brcs_lut_range_error. Unable to index into BRCS uncertainty lookup table.
					16777216/0x01000000 (Bit 25) = ant_data_lut_range_error. Unable to index into antenna data lookup table.
					33554432/0x02000000 (Bit 26) = bb_framing_error. Insufficient black body data for calibration.
					67108864/0x04000000 (Bit 27) = fsw_comp_shift_error. Flight software telemetry encoding error of the fsw_comp_delay_shift and fsw_comp_dopp_shift variables. Corrected in FSW version 4.5.



					134217728/0x08000000 (Bit 28) = low_quality_gps_ant_knowledge: Not enough data is available to properly calibrate the NBRCS for this sample's GPS satellite.
					268435456/0x10000000 (Bit 29) = sc_altitude_out_of_nominal_range: The spacecraft's altitude is out of nominal altitude range. Nominal altitude is defined as between 490 km to 550 km.
					536870912/0x20000000 (Bit 30) = anomalous_sampling_period: Set when an anomaly was observed on the CYGNSS or GPS satellite while this sample was taken. These samples have produced data that do not align with typical CYGNSS results. See up to date list at: https://docs.google.com/spreadsheets/d/1AFAZanVGDApLSnJQAAdPfOKoJQs0jnB8ZvIuD1Z5mAc/edit?usp=sharing
					1073741824/0x40000000 (Bit 31) = invalid_roll_state: The spacecraft's reported roll angle is more than 1 degree from the commanded roll.
quality_flags_2	Per-DDM quality flags 2	int	<none>	sample, ddm	Second group of the Per-DDM quality flags. 1 indicates presence of condition. The first group of quality flags can be found in quality_flags. Flag bit masks:
					1/0x00000001 (Bit 01) = incorrect_ddmi_antenna_selection: The wrong (port or starboard) antenna was selected.
					2/0x00000002 (Bit 02) = high_signal_noise: The signal is in the highest noise group, but there are still some OK noise rows. Samples are suspect, but may contain quality data. Flag only used for land applications.



					4/0x00000004 (Bit 03) = noise_floor_cal_error: The signal is off or is very near the top rows of the full DDM. A proper noise floor cannot be computed. Flag only used for land applications.
					8/0x00000008 (Bit 04) = sp_in_sidelobe: The specular point is in the sidelobe causing low confidence in the antenna gain.
					16/0x00000010 (Bit 05) = negligible_nst_outage: Minor star track outage with negligible impact on attitude knowledge
					32/0x00000020 (Bit 06) = minor_nst_outage: Minor star track outage with small but acceptable impact on attitude knowledge
					64/0x00000040 (Bit 07) = fatal_nst_outage: Star track outage with unacceptable impact on attitude knowledge
					128/0x00000080 (Bit 08) = low_zenith_ant_gain: Zenith antenna gain is less than -6 dB
					256/0x00000100 (Bit 09) = poor_bb_quality: The distance between the surrounding BB samples > 1350 seconds OR the absolute value of the time to the nearest BB > 350 seconds.
					512/0x00000200 (Bit 10) = poor_quality_bin_ratio: Bin ratio on the nadir or zenith antenna is associated with degraded performance.
Per-Bin Values					
raw_counts	DDM bin raw counts	int	1	sample, ddm, delay, doppler	17 x 11 array of DDM bin raw counts. These are the uncalibrated power values produced by the DDMI.
power_analog	DDM bin analog power	float	watt	sample, ddm, delay, doppler	17 x 11 array of DDM bin analog power, Watts. analog_power is the true power that would have been measured by an ideal (analog) power sensor.



					<p>power_digital is the power measured by the actual 2-bit sensor, which includes quantization effects.</p> <p>power_analog has been corrected for quantization effects.</p>
brcs	DDM bin bistatic radar cross section	float	meter ²	sample, ddm, delay, doppler	<p>17 x 11 array of DDM bin bistatic radar cross section, m². The specular point is located in DDM bin</p> <p>round(brcs_ddm_sp_bin_delay_row),</p> <p>round(brcs_ddm_sp_bin_dopp_col).</p>
eff_scatter	DDM bin effective scattering area	float	meter ²	sample, ddm, delay, doppler	<p>17 x 11 array of DDM bin effective scattering area, m². This is an estimate of the true surface scattering area that contributes power to each DDM bin, after accounting for the GPS signal spreading function. It is calculated by convolving the GPS ambiguity function with the surface area that contributes power to a given DDM bin as determined by its delay and Doppler values and the measurement geometry. The specular point bin location matches the specular point bin location in brcs.</p>